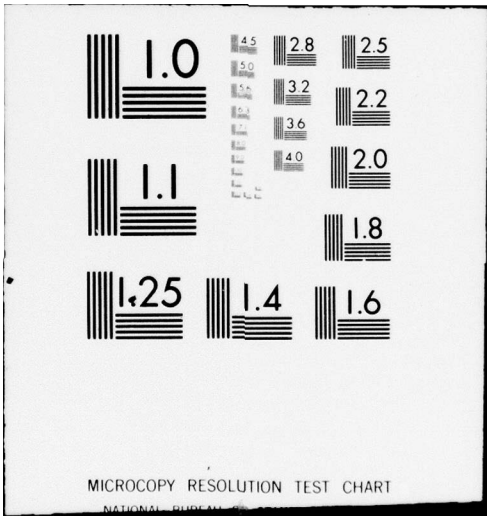
AD-A077 904 NAVAL RESEARCH LAB WASHINGTON DC F/G 20/4
HYDRODYNAMICS OF GAS CHANNEL FORMATION.(U)
OCT 79 M LAMPE , H H SZU , S KAINER
UNCLASSIFIED NRL-MR-4073 NL

| OF |
AD A
077904



END
DATE
FILMED
1-80
DDC


1.0
1.1
1.25
1.4
1.6
1.8
2.0
2.2
2.5
2.8
3.2
3.6
4.0
4.5
5.0
MICROCOPY RESOLUTION TEST CHART

LEVEL II

NRL Memorandum Report 4073

AD A077904

Hydrodynamics of Gas Channel Formation

MARTIN LAMPE, H. HAROLD SZU, AND SELIG KAINER

Plasma Theory Branch
Plasma Physics Division

October 25, 1979

DDC FILE COPY



DDC
RECEIVED
DEC 11 1979
A

NAVAL RESEARCH LABORATORY
Washington, D.C.

Approved for public release; distribution unlimited.

79 12 6 129

SECURITY CLASSIFICATION OF THIS PAGE (When Data Entered)

REPORT DOCUMENTATION PAGE

READ INSTRUCTIONS BEFORE COMPLETING FORM

1. REPORT NUMBER: NRL Memorandum Report 4073	2. GOVT ACCESSION NO.
3. RECIPIENT'S CATALOG NUMBER: NRL-MR-4073	
4. TITLE (and Subtitle): HYDRODYNAMICS OF GAS CHANNEL FORMATION	5. TYPE OF REPORT & PERIOD COVERED: Interim report on a continuing NRL problem.
	6. PERFORMING ORG. REPORT NUMBER
7. AUTHOR(s): Martin Lampe, H. Harold Szu and Selig Kainer	8. CONTRACT OR GRANT NUMBER(s)
9. PERFORMING ORGANIZATION NAME AND ADDRESS: Naval Research Laboratory, Washington, D.C. 20375	10. PROGRAM ELEMENT, PROJECT, TASK AREA & WORK UNIT NUMBERS: NRL Problem R08-93B
11. CONTROLLING OFFICE NAME AND ADDRESS: Naval Surface Weapons Center, White Oak, Silver Spring, Maryland 20910	12. REPORT DATE: October 25, 1979
	13. NUMBER OF PAGES: 67
14. MONITORING AGENCY NAME & ADDRESS (if different from Controlling Office)	15. SECURITY CLASS. (of this report): Unclassified
	15a. DECLASSIFICATION/DOWNGRADING SCHEDULE

16. DISTRIBUTION STATEMENT (of this Report)

Approved for public release; distribution unlimited.

17. DISTRIBUTION STATEMENT (of the abstract entered in Block 20, if different from Report)

18. SUPPLEMENTARY NOTES

This research was sponsored by the Naval Surface Weapons Center under subtask N60921-79-WR-W0186.

19. KEY WORDS (Continue on reverse side if necessary and identify by block number)

Charged Particle Beam
Hydrodynamics
Gas Channel Formation
Hole Boring

20. ABSTRACT (Continue on reverse side if necessary and identify by block number)

The hydrodynamic response of a gaseous medium to the passage of a series of brief, widely spaced, well collimated energy pulses (e.g. electron beam pulses, laser pulses, discharges, etc.) is studied. Fluid code simulations are reported over a wide range of parameters. Iterative analytic formulae are given for the density reduction profile resulting from each pulse. Shock production and heating, as well as other dynamic effects, are included.

DD FORM 1 JAN 73 1473 EDITION OF 1 NOV 65 IS OBSOLETE
S/N 0102-014-6601

251 950

CONTENTS

I. INTRODUCTION 1

II. GAS EXPANSION FOLLOWING PASSAGE OF A SINGLE PULSE 5

A. General Remarks 5
B. Final State 7
C. Shock Formation and Entropy Increase 9
D. Time Evolution 13

III. EXPANSION FOLLOWING ENERGY DEPOSITION IN A PRE-EXCITING CHANNEL 15

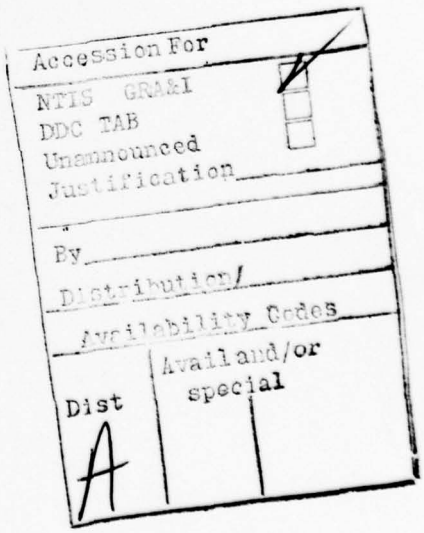
A. General Remarks 15
B. Pulse-to-Pulse Evolution of Channel Density 17
C. Time Evolution 20

IV. WEAK BEAM PULSE—LINEARIZED HYDRODYNAMICS 21

V. CONCLUSIONS 26

ACKNOWLEDGMENTS 28

REFERENCES 28



Hydrodynamics of Gas Channel Formation

1. INTRODUCTION

There has been interest recently in the formation of heated, reduced-density channels in gaseous media, by passing a laser pulse,[1] an electron beampulse,[2] an electric discharge,[3] or an exploding wire current[4] through the gas. Such a channel may be used to guide a charged particle beam from the beam source to a fusion pellet in an inertial confinement fusion reactor. In some cases, it may also be possible to pulse the channel several times by passing widely spaced energy pulses through it.

In this report, we study specifically the hydrodynamics of channel formation. Analytic solutions have been obtained in the past for blast wave hydrodynamics in cylindrical geometry,[5] but only for strong blast waves (where the shock has high Mach number, even after it has expanded to many times the initially heated radius). Such solutions are valid only if the initial overpressure is hundreds or thousands of times the ambient pressure. Our interest here is in more moderate overpressures. One-dimensional fluid code simulations of the radial gas hydrodynamics are presented, over a wide range of parameters. Theoretical arguments, as well as scaling laws induced from the simulations, are used to construct analytic models which include all the qualitative features of channel hydrodynamics, and permit accurate quantitative calculation of the process without further resort to hydrodynamic codes. In order to focus as clearly as

Manuscript submitted July 11, 1979.

possible on the hydrodynamics, we avoid getting into beam propagation and energy deposition, late-time channel cooling, and the complications of real gas thermal properties.

We consider the case in which the duration of the heating pulse is so short that it can be treated as instantaneous on the hydrodynamic time scale. In the case of multiple heating pulses, we treat the regime in which pulse spacing is long enough so that low density gas channel will have (or nearly have) come to rest, in pressure balance with the ambient gas, by the time the next pulse arrives. Thus the hydrodynamic process is an interative one, in which each pulse serves only to leave behind an essentially static channel, i.e., an initial condition for the next stage of channel expansion. Thus the problem we set for ourselves is as follows. Given a gas density profile $\rho_{n-1}(r,\ t_n = 0)$, created by the first $n-1$ pulses; t_n is time measured with $t_n = 0$ at the arrival time of the n^{th} pulse. Given also a pressure profile $P_n(r,\ t_n = 0^+) = P_{n-1}(r) + P_n'(r)$, where $P_{n-1}(r)$, which is close to the ambient pressure, is due to the previous pulses, and $P_n'(r)$ is the overpressure profile due to energy deposition at $t_n = 0$ by the n^{th} pulse. We calculate the subsequent hydrodynamic response of the gas.

The properties of the heating source (laser, electron beam, or whatever) appear in our calculations only through the "initial" overpressure profile, after the passage of the n th pulse, $P_n'(r)$. For specificity we assume a Bennett profile, $P_n'(r) = \dfrac{P_{on}}{(1 + r^2/a^2)^2}$, a typical smooth bell-shaped profile which is particularly appropriate for an electron beam under certain conditions.[6] We shall extend this work to consider arbitrary profiles in a subsequent paper.

A further simplification is made in the presentation here, by taking the adiabatic index of the gas, $\gamma \equiv C_p/C_v$, to be constant (where C_p and C_v are the specific heats at constant pressure and volume). In numerical work, we assume specifically $\gamma = 7/5$, the value appropriate to a

diatomic gas without internal degrees of freedom. In real gases, γ can vary considerably at high temperatures, where internal degrees of freedom are excited; such complications will be included in future work.

The principal results of this report will be summarized in the remainder of this section. Section 2 presents the detailed simulation and theory for a first pulse, fired into a homogeneous gas. Section 3 gives analogous results for a pulse depositing its energy in a preformed channel. Section 4 deals with the special case of a weak pulse, which results in an overpressure small compared to the ambient pressure; in this case, the channel formation process reduces to linear sound wave propagation, and the complete time-dependent hydrodynamics can be solved in closed form. Section 5 briefly summarizes our conclusions.

In order to elucidate the scaling laws, it is best to deal with the channel formation process in dimensionless variables, scaled to ambient values, with r scaled to heating-source (or "beam") radius a, and t scaled to a/c_s, wherer c_s is ambient sound speed. These dimensionless variables are denoted by tildes. Table 1 summarizes the notation used throughout the paper.

The hydrodynamic processes following the passage of a beam pulse with a Bennett profile can be separated into three phases, on different time scales: (1) First, gas density reduction by a rarefaction wave within the beam radius (2) Expansion and density reduction within the rarefied channel, which is typically several times larger than the beam radius. In general, the channel as a whole reaches a minimum density state, when the pressure throughout it is (over a wide range of parameters) about 85-90% of ambient pressure. (3) Slow return of the channel to ambient pressure, with an accompanying density increase of about 10%. The time scales for these processes are summarized in Table 2.

If the pulse separation is long enough so that the channel reaches a stationary state between pulses, the hydrodynamic process is an iterative one, in which the density profile $\rho_n(r)$ after n pulses can be expressed in terms of the previous channel profile, $\rho_{n-1}(r)$, and the overpressure on axis due to the n^{th} pulse, P_{on}. The density reduction at $r = 0$ (and, in general, for $r \lesssim a$) is due simply to adiabatic expansion, and can be expressed in a very simple analytic form. In fact, adiabatic expansion is a fairly reasonable model for the channel profile as a whole, but the density channel is widened by up to $\sim$20% per pulse by additional heating, due to a radially outward-propagating shock driven by each heating pulse. The results for the density profile reached, when the channel comes to rest after the n^{th} pulse, are summarized in Table 3.

If the pulses are spaced such that each one arrives when the channel is at minimum density (at pressure 10-15% below ambient), then the density profiles, at the time when the n^{th} pulse arrives, are simply depressed below the results of Table 3 by about 10%. This effect does not increase cumulatively from pulse to pulse.

Finally, we note that for an initial Bennett overpressure profile, the channel does not undergo repeated strong radial oscillations after heating by any given pulse. Rather, its density dips, only once, about 10% below its final value, and then slowly returns to its final value. If "ringing" of the channel occurs, it is at very small amplitude.

Figures 1.1 through 1.3 give a quick sample of some results derived by the analytic arguments described above. Fig. 1.1 shows the central density when the gas comes to rest after the first pulse, as a function of the central overpressure $\tilde{P}_o$. Figure 1.2 shows the coordinate $\tilde{r}_1$ of

the fluid element that originated at $\tilde{r} = 1$, when the gas comes to rest after the first pulse. Figure 1.3 shows a graphical method of calculating the location of any given fluid element, when the gas comes to rest after the first and second pulses.

II. GAS EXPANSION FOLLOWING PASSAGE OF A SINGLE PULSE

A. General Remarks

In this section we present extensive numerical solutions for the radial expansion of the gas following the passage of a single pulse, outline the principal features of this hydrodynamic evolution, and present analytical and heuristic techniques that treat all of these features and permit quantitative calculation of the evolution by much simpler methods. For simplicity, we assume a constant value for the ratio of specific heats $\gamma = c_p/c_v$, and choose $\gamma = 7/5$, as is appropriate for a diatomic gas in the absence of internal degrees of freedom. We assume that the gas is initially heated by the (essentially instantaneous) passage of the pulse, and that the initial heating profile is the Bennett profile, i.e., the initial conditions for density ρ, pressure P, and temperature T are

$$\rho(r,0) = \rho_A, \tag{2.1}$$

$$P(r,0^+) = P_A\left[1 + \frac{\tilde{P}_0}{(1+r^2/a^2)^2}\right], \tag{2.2}$$

$$T(r,0) = T_A\,\frac{P(r,0^+)}{P_A}, \tag{2.3}$$

where the subscript A denotes ambient values. Thermal conduction and radiative cooling are neglected, since they proceed much slower than the hydrodynamic evaluation. The only dissipation included in the model is that which occurs in shocks; the latter is treated in a manner

which reproduces the Rankine-Hugoniot relations with great accuracy, without resorting to the (sometimes troublesome) numerical artifice of a Von Neumann viscosity.

It is natural to treat this problem in dimensionless units

$$\tilde{r} = r/a, \tag{2.4a}$$

$$\tilde{t} = tc_A/a, \tag{2.4b}$$

$$\tilde{\rho} = \rho/\rho_A, \ \tilde{P} = P/P_A \tag{2.5}$$

where a is the Bennett radius and $c_A \equiv (\gamma P_A/\rho_A)^{1/2}$ is the ambient sound speed. In terms of these units, the evolution depends only on the single dimensionless parameter $\tilde{P}_o$, the initial overpressure at $r = 0$, scaled to the ambient pressure. For example, if the Bennett radius a is halved, but the total energy deposited is held constant, then $\tilde{P}_o$ is quadrupled.

This initial value problem has been solved numerically for a wide range of values of $\tilde{P}_o$. The one-dimensional (radial) code ETBFCT was used to solve the Euler hydrodynamic equations (conservation equations of mass, momentum and energy) in conservative form. The code is Eulerian, with non-uniform grid spacing and regridding capability to enhance accuracy near the origin and at the shock location. The code uses the flux-conserving transport (FCT)[7] technique, and has been tested extensively to verify its accuracy in treating shocks in non-uniform media.[8] It has been shown to reproduce the jump conditions across a discontinuity (i.e. the Rankine-Hugoniot conditions across a shock) with extraordinary accuracy, if one looks several cells downstream from the shock. However, some averaging occurs over two or three cells at the shock, which numerically clips the density and pressure peak at the shock, preventing one from accurately reading off the shock strength in a strongly non-uniform case. This effect is reduced (to a factor $\lesssim 1.2$ in our computer runs) by using a fine grid spacing near the shock. In the various figures showing density and pressure profiles, we have extrapolated the numerical results to reconstruct sharp peaks at the shocks.

The time evolution of the density and pressure profiles is shown in Figs. 2.1-8, for cases with $\tilde{P}_o = 42.0$, 10.5, 1.8, and 0.1. In all cases, the following sequence of events occurs. (i) A pressure-density pulse forms on the outside of the heated gas region, and begins to move out radially. A rarefaction forms behind this pressure pulse, causing the central density to drop. (ii) For a smooth (e.g. Bennett) initial pressure profile, the density and pressure pulses are initially smooth, but steepen to a shock wave after a finite time* which will be estimated theoretically in Sec. 2C. 1 The shock strength (indicated, e.g., by the density jump) grows for a while, reaches a maximum, and then falls off because of the cylindrical expansion. (iii) Behind the shock, a low-density channel forms, the temperature decreases somewhat from its initially high value because of PdV work done against the ambient presure, and the pressure falls until it reaches the ambient level. (iv) The shock eventually detaches from the channel, and propagates toward $r = \infty$, carrying part of the initially deposited energy with it. (v) Meanwhile, the density in the channel undershoots pressure equilibrium with the ambient gas by a small amount, and then the density and pressure increase very slowly until pressure equilibrium is reached. The density channel does *not* undergo a series of violent oscillations about pressure equilibrium such as occurs in the well-known case of an underwater explosion,[9] i.e., a high-pressure gas bubble formed in an essentially incompressible medium. On the contrary, only a single, weak overshoot of equilibrium occurs.

B. Final State

The density profile at late times, after the gas has come to rest in pressure equilibrium, can be expressed in terms of the initial state and the properties of the shock. The specific entropy of a gas is expressed in terms of γ as

*In the cases of weak initial heating, the shock is so weak that it is difficult to resolve, and is of no real importance.

$$S = c_v \ln (P\rho^{-\gamma}). \tag{2.6}$$

In our system, dissipation occurs only in the shock front. Any given element of fluid is overrun by the shock no more than once. If we let $\Delta S(r_o)$ be the specific entropy increase when the shock crosses the fluid element whose *initial* position was r_o, then Eq. (2.6) can be rewritten as

$$\tilde{\rho}(r_o,t) = \left[\frac{\tilde{P}(r_o,t)}{\tilde{P}(r_o,0^+)}\right]^{1/\gamma} \exp\left[-\Delta S(r_o)/c_p\right], \tag{2.7}$$

where we use the dimensionless variables (2.5). In Eq. (2.7), r_o is used as a Lagrangian coordinate, i.e., a label for the fluid element located at r_o at $t = 0$. The Eulerian coordinate r, i.e., the position of this fluid element at time t, can be regarded as a function of r_o and t. At $t = \infty$ in particular,

$$\tilde{P}(\tilde{r}_o,\infty) = 1,$$

and

$$\begin{aligned}\tilde{\rho}(\tilde{r}_o,\infty) &= [\tilde{P}(\tilde{r}_o,0^+)]^{-1/\gamma} \exp\left[-\Delta S(\tilde{r}_o)/c_p\right] \\ &= \left\{1 + \frac{\tilde{P}_o}{(1+\tilde{r}_o^2)^2}\right\}^{-1/\gamma} \exp\left[-\Delta S(\tilde{r}_o)/c_p\right].\end{aligned} \tag{2.8}$$

In (2.8), we use also a dimensionless Lagrangian coordinate,

$$\tilde{r}_o \equiv r_o/a. \tag{2.9}$$

Since Eqs. (2.7), (2.8) are written in terms of the Lagrangian coordinate $\tilde{r}_o$, the Eulerian coordinate $\tilde{r}(\tilde{r}_o,\tilde{t})$ must be prescribed to complete the description. This is accomplished by noting that the volume element $d(\pi r^2)$ is inversely proportional to the density ρ, so that

$$\frac{\partial^2}{\partial \tilde{r}_o^2}\,\tilde{r}^2(\tilde{r}_o,\tilde{t}) = \frac{\rho(\tilde{r}_o,0)}{\rho(\tilde{r}_o,\tilde{t})} = \frac{1}{\tilde{\rho}(\tilde{r}_o,\tilde{t})}, \tag{2.10a}$$

hence

$$\tilde{r}^2(\tilde{r}_o,\tilde{t}) = \int_0^{\tilde{r}_o^2} d(\tilde{r}_o')^2/\tilde{\rho}(\tilde{r}_o',\tilde{t}). \tag{2.10b}$$

or, in particular, at late times,

$$\tilde{r}^2(\tilde{r}_o,\infty) = \int_0^{\tilde{r}_o^2} d(\tilde{r}_o')^2/\tilde{\rho}(\tilde{r}_o',\infty). \tag{2.10c}$$

Equations (2.8) and (2.10c) completely specify the density profile at $t = \infty$, once ΔS is known.

Since the shocks are rather weak, even for overpressures up to $\tilde{P} = 42$ (as will be discussed in Sec. 2c), the approximation

$$\Delta S = 0 \tag{2.11}$$

is qualitatively reasonable. (We shall see that it is exact within the central channel.) If this approximation is made, Eq. (2.8) reduces to

$$\tilde{\rho}(\tilde{r}_o,\infty) = [\tilde{P}(\tilde{r}_o,0^+)]^{-1/\gamma} = \left[1 + \frac{\tilde{P}_o}{(1+\tilde{r}_o^2)^2}\right]^{-1/\gamma} \tag{2.12}$$

and Eqs. (2.10c) and (2.12) give a very simple first approximation to $\tilde{\rho}(\tilde{r},\infty)$. This result is plotted as solid curves in Figs. 2.9-2.12, for the various values of $\tilde{P}_o$, along with the computed density profiles at late time. We note that the approximation of Eqs. (2.10c,12) predicts the depth of the central density hole exactly, after the gas has come to pressure equilibrium. However, the approximation underestimates the width of the density channel by up to 20% in the strongest case. Of lesser importance, the approximation fails to predict a broad, very shallow ($\lesssim$ 5%) wing to the density channel. As will be discussed, the channel is wider, but not deeper, than the isentropic model prediction, because only the outer regions are shock-heated.

C. Shock Formation and Entropy Increase

We note first that the radially outward-propagating shock forms at some radial position $\tilde{r}_s$, and overruns all of the gas outside $\tilde{r}_s$. The central region $\tilde{r} < \tilde{r}_s$ is never overrun by a shock, and its expansion is thus isentropic, and given by Eqs. (2.10c) and (2.12), in agreement with

the fluid code results. The code runs indicate that the shock forms in the fluid element whose initial (i.e., Lagrangian) coordinate is

$$\tilde{r}_o = \tilde{r}_{os} \sim 0.8; \tag{2.13}$$

this will shortly be explained theoretically. Thus the entire central region of the low density channel (e.g., out to $\tilde{r} \sim 3$ after expansion has occurred, for $\tilde{P}_o = 42$) should be, and is, accurately predicted at $t = \infty$ by Eqs. (2.10c) and (2.12).

We next discuss the determination of $\tilde{r}_{os}$, in a qualitative way. Any hydrodynamic disturbance will eventually steepen and form a shock, but the time t_s necessary for this to occur varies inversely with the strength of the disturbance. We know of no general formula for t_s (except in the idealized case of a Riemann simple wave) but we can construct an approximate formula as follows. An idealized pressureless fluid free streams according to its initial velocity distribution, i.e., satisfies the equation

$$\frac{\partial u}{\partial t} + \frac{\partial u}{\partial r} = -\frac{1}{\rho}\frac{\partial P}{\partial r} = 0, \tag{2.14a}$$

or equivalently,

$$u(r, t) = u(r - u(r, t)t). \tag{2.14b}$$

It can be shown exactly[10] that, according to this model, a shocklike discontinuity forms in each fluid element whose initial location r_{os} is such that $\dfrac{\partial u(r_o, 0)}{\partial r_o}$ is a minimum, and at time

$$t = \left[\frac{\partial u(r_o, 0)}{\partial r_o}\right]^{-1}_{r_o = r_{os}}. \tag{2.15}$$

However, in the real problem under consideration, the initial velocity is zero everywhere, and it takes a finite time for the velocity field to develop; also, the velocities continue to change under the influence of pressure gradients. But if the shock forms before the pressure profile is greatly changed, which occurs if the pressure perturbation is strong, then it is reasonable qualitatively

to picture shock formation as a two-stage process: during a period τ_1, a velocity profile $u(r)$ develops out of the *initial* pressure profile $P(r, 0)$, and during a subsequent time τ_2, this velocity profile free-streams until it steepens to a shock. The shock formation time is then

$$t_s = \tau_1 + \tau_2. \tag{2.16}$$

At time τ_1, according to this picture,

$$u(r, \tau_1) \approx -\int_o^{\tau_1} \frac{dt}{\rho} \frac{\partial P(r, t)}{\partial r} \approx -\frac{\tau_1}{\rho_A} \frac{\partial P(r, 0^+)}{\partial r}, \tag{2.17}$$

and according to Eq. (2.15), τ_2 is given by

$$\tau_2 \approx Min_r \left|\frac{\partial u(r, \tau_1)}{\partial r}\right|^{-1} \approx Min_r \frac{\rho_A}{\tau_1} \left|\frac{\partial^2 P(r, 0^+)}{\partial r^2}\right|^{-1}, \tag{2.18}$$

where the notation $\min_r$ devotes the minimum with respect to r. But τ_1 is arbitrary in this picture; therefore one may choose τ_1 such as to minimize t_s, i.e.,

$$t_s = Min_{\tau_1} Min_r \left\{\tau_1 + \frac{\rho_A}{\tau_1} \left|\frac{\partial^2 P(r, 0^+)}{\partial r^2}\right|^{-1}\right\}. \tag{2.19}$$

Performing the minimization over τ_1, we find

$$\tau_1 = \rho_A^{1/2} \left[Max_r \left|\frac{\partial^2 P(r, 0^+)}{\partial r^2}\right|\right]^{-1/2} \tag{2.20a}$$

and

$$t_s = 2\rho_A^{1/2} \left[Max_r \left|\frac{\partial^2 P(r, 0^+)}{\partial r^2}\right|\right]^{-1/2}. \tag{2.20b}$$

The shock forms in the fluid element whose initial position r_{os} is determined by

$$\frac{\partial^3 P(r_o, 0)}{\partial r_o^3}\Big|_{r_{os}} = 0. \tag{2.21}$$

For the assumed Bennett profile of $P(r_o, 0)$, we find

$$\tilde{r}_{os} = (3/5)^{1/2} = 0.78, \tag{2.22a}$$

$$\tilde{t}_s = 2.14\, \tilde{P}_o^{-1/2}. \tag{2.22b}$$

These estimates of $\tilde{t}_s$ and $\tilde{r}_{os}$ are found to be in reasonable agreement with the fluid code results for $\tilde{P}_o \gtrsim 5$, as seen in Figs. 1 and 2. For the weaker overpressures, the actual shock onset time can be much later than these estimates, but in these cases the shock is so weak as to be insignificant anyway.

When it first forms at time t_s, the shock is very weak. As a result, there is no discernible discontinuity in the final density profile $\tilde{\rho}(\tilde{r}_o, \infty)$ between the unshocked region $\tilde{r}_o < \tilde{r}_{os}$ and the shocked region $\tilde{r}_o > \tilde{r}_{os}$. After its initial formation, the shock propagates outward and continues to grow, as additional fluid piles up behind it. It reaches a maximum amplitude at Lagrangian coordinate $\tilde{r}_{om}$, and then its amplitude decreases, as its area increases because of cylindrical expansion. Theoretical results for the variation of shock amplitude exist in the literature for the self-similar (blast wave) expansions that occur for very strong overpressures,[5] but these results apply for Mach numbers $M >> 1$, for which the density jump ρ^-/ρ^+ across the shock approaches six. They are not particularly valid even for the strongest overpressure studied here, $\tilde{P} = 42$, for which $M \lesssim 2.4$ and $\rho^-/\rho^+ \lesssim 3.3$. As discussed in Sec. IIA, it is also difficult to plot the shock amplitude evolution accurately from the fluid code results. However, a heuristic estimate of shock strength has been found, which agrees with the code results to within their accuracy, for cases where the shock is strong enough to be significant ($P_o \gtrsim 5$). This permits accurate calculation of the final density profile, and correctly represents the shock onset from Eq. (2.22a), and the fact that, for $\tilde{r}_o$ large, shock stength should depend on $\tilde{P}_o$ and $\tilde{r}_o$ only through the combination $\tilde{P}_o \tilde{r}_o^{-2}$, i.e., the ratio of overpressure energy $P_o a^2$ to ambient thermal energy $P_A r_o^2$. It is convenient to express the shock strength in terms of the density jump ρ^-/ρ^+ across the shock:

$$\rho^-/\rho^+ \approx \begin{cases} 1 & \tilde{r}_o < 0.8 \\ 1 + 0.33\, \tilde{P}_o^{1/4}\, \tilde{r}_o, & 0.8 \leqslant \tilde{r}_o < 3 \\ 1 + 1.7\, \tilde{P}_o^{1/4}\, r_o^{-1/2}, & 3 \leqslant \tilde{r}_o \end{cases} \tag{2.23}$$

The entropy jump $\Delta s(r_o)$ and the Mach number M are related to ρ^-/ρ^+ through

$$\exp(-\Delta S/c_p) = \frac{\rho^-}{\rho^+}\left(\frac{P^+}{P^-}\right)^{1/\gamma} = \frac{\rho^-}{\rho^+}\left(\frac{6-\rho^-/\rho^+}{6\rho^-/\rho^+ - 1}\right)^{5/7}, \tag{2.24}$$

$$M^2 = \frac{5\rho^-/\rho^+}{6-\rho^-/\rho^+}. \tag{2.25}$$

The entropy jump $\Delta S(r_o)$ from Eqs. (2.23), (2.24) can be used with Eqs. (2.8), (2.10c) to provide a complete calculational model for the final density profile, when the channel reaches pressure equilibrium. It can be seen in Figs. 2.9 and 2.10 that the agreement with the fluid code results is very good.

D. Time Evolution

Thus far, we have been concerned primarily with obtaining accurate estimates of the density profile $\rho(r, \infty)$ at late times, when the pressure $P(r, \infty)$ has returned to ambient. In this section, we shall consider the time scales for radial expansion, and the minimum density that occurs during the evolution. It is difficult to obtain theoretical results in this area, but analysis of the fluid code solutions yields some simple heuristic generalizations.

We note, from Figs. 2.1-2.4, that the density in the channel reaches a minimum during the evolution, and then slowly returns to its final equilibrium value. When viewed in terms of the pressure profile, as in Figs. 2.5-2.8, this undershoot takes a very simple form in the whole range $\tilde{P}_o \gtrsim 1$. In all of these cases, the pressure profile $P(r, t)$ takes on a very broad, shallow minimum value P_m, slightly below P_A, at some time t_m. Since $P(r)$ is practically constant over the density channel, the density profile at t_m is given by Eqs. (2.8), (2.10c), simply by replacing P_A with P_m, i.e.,

$$\tilde{\rho}(\tilde{r}_o, \tilde{t}_m) = \tilde{P}_m^{1/2}\left(1 + \frac{\tilde{P}_o}{(1+\tilde{r}_o^2)^2}\right)^{-1/\gamma} \exp\left[-\Delta S(r_o)/c_P\right], \tag{2.26}$$

and

$$\tilde{r}^2(\tilde{r}_o,\ \tilde{t}_m) = \int_0^{\tilde{r}_o^2} d(\tilde{r}_o')^2 / \tilde{\rho}(\tilde{r}_o',\ \tilde{t}_m). \tag{2.27}$$

The pressure minimum $\tilde{P}_m$ is plotted as a function of $\tilde{P}_o$ in Fig. 13. It is seen to be very slowly varying over the whole range $\tilde{P}_o \gtrsim 1$; one is not far off in estimating $\tilde{P}_m = 0.88$ for all such values of $\tilde{P}_o$. Thus, in Lagrangian coordinates, the minimum density $\tilde{\rho}(\tilde{r}_o,\ \tilde{t}_m)$ is approximately 10% less than the equilibrium profile $\tilde{\rho}(\tilde{r}_o,\ \infty)$. In Eulerian coordinates, the effect is greater, since the channel itself is also widened by approximately a factor $(1.10)^{1/2} \approx 1.05$.

This particularly simple picture cannot hold in the regime $\tilde{P}_o << 1$, where all perturbed quantities, e.g., $1 - \tilde{P}_m$, must be linearly proportional to $\tilde{P}_o$ (as shown in Fig. 2.13). If $\tilde{P}_o << 1$ the channel formation process becomes one of linear sound wave propagation. In such a process, the pressure profile is of similar width (rather than much broader) to the density profile. A complete time-dependent analytic solution for the linear case $\tilde{P} << 1$ is given in Sec. IV.

The time evolution of the density channel can be divided roughly into three stages. Rapid radial expansion occurs at early times in the central region $\tilde{r} \lesssim 1$, initially at the inital local sound speed $c(\tilde{r} = 0,\ \tilde{t} = 0)$, but later slowing down to the ambient sound speed. In the second stage, expansion occurs at a velocity only moderately higher than the ambient sound speed, over a region corresponding to the final channel size, i.e., a low Mach number shock propagates over this region. In the third stage, the channel returns very slowly from its minimum density state to the final equilibrium. This evolution may be seen in Figs. 2.1-2.8. The data is also replotted in compact form in Figs. 2.14 and 2.15, where the time dependence of $\rho(r = 0)$, and of the shock radius $\tilde{R}_s(\tilde{t})$ are shown.

We note from Fig. 2.14 a very simple rule that essentially determines the end of the first stage, and tells us how long it takes for the central channel to be created: the change in density is 90% complete* when* $\tilde{t} \approx 0.7$, independent of $\tilde{P}_o$. It takes much longer for the remaining density reduction to be accomplished, essentially because expansion over a larger volume is involved, and the overpressure becomes weak.

The second stage can be said to terminate when minimum density is reached; this time $\tilde{t}_m$ increases with $\tilde{P}_o$ because the size of the low-density channel increases, and is given accurately (to within $< 10\%$ for all values of $\tilde{P}_o$ studied) by the simple formula $\tilde{t}_m = 1.2 \times (\tilde{P}_o + 1)^{1/2}$.

The duration of the third stage, i.e., the return to pressure equilibrium, is essentially the time for sound to propagate at the ambient rate over the reduced pressure region. Typically the return to equilibrium has an e-folding time of about $1.5\tilde{t}_m$.

III. EXPANSION FOLLOWING ENERGY DEPOSITION IN A PRE-EXCITING CHANNEL

A. General Remarks

If the channel is heated repeatedly by a series of energy pulses, and if the separation between pulses is so long that the channel essentially comes to rest between pulses, in pressure balance with the ambient gas, then the hydrodynamic expansion process is an iterative one, in which the final channel state, after the previous pulse, consitutes the initial density profile for the next stage of expansion. The first pulse is uniquely simple in that it deposits its energy in homogeneous gas; this makes possible the unambiguous choice of dimensionless coordinates as

* But note that if $\tilde{P}_o$ is very large, then the final 10% of the density reduction results in further reduction of density by a significant factor, e.g., if $\tilde{p}(r = 0.1$, the factor is 2.

in Eqs. (2.4, 2.5), based on the spatial scale a and the time scale a/c_A. For a pulse depositing energy in a proformed channel, the subsequent hydrodynamic expansion depends on both the beam and channel radii, as well as on the overpressure; furthermore, the time scales depend on the *local* sound speed in the pre-existing heated, low-density channel, as well as on the ambient sound speed. Thus it is no longer possible to reduce the hydrodynamic behavior to a one-parameter problem by choosing an obvious set of dimensionless coordinates. Nevertheless, we shall see that the calculation of the channel configuration, after it comes to rest in pressure balance, can be extended to the present case, and much of the analysis of shock properties, pressure undershoot, and time scales can be extended in a qualitative way. We also consider cases in which the pulse separation is such that the channel has reached a uniform pressure which is near (but not quite at) ambient pressure when the next pulse arrives.

We continue to assume for specificity that the overpressure caused by the n^{th} pulse in a pre-existing channel has a Bennett profile, with Bennett radius a. As in Sec. 2, Eqs. (2.4), we adopt dimensionless units in which radial distances are scaled to a, times to a/c_A (where c_A is the ambient sound speed), and densities, pressures, and temperatures to ρ_A, P_A, and T_A. Such dimensionless quantities are identified by tildes. In addition, it is now convenient to define quantities referred specifically to the time $\tilde{\tau}_n$ of arrival of the n^{th} pulse. We define $\tilde{t}_n = \tilde{t} - \tilde{\tau}_n$ as the dimensionless time, so that $\tilde{t}_n = 0$ at the time of arrival of the n^{th} pulse. Also, we define $\tilde{r}_{n-1}$ (scaled to a) as the dimensionless coordinate of a particular element fluid at $\tilde{t}_n = 0$. As with $\tilde{r}_o$ in Sec. 2, $\tilde{r}_{n-1}$ is used as a Lagrangian coordinate, i.e., a label for an element of gas. In the case of a series of beam pulses, one can use $\tilde{r}_o$ as the Lagrangian coordinate while following the hydrodynamics after the first pulse, $\tilde{r}_1$ as the Lagrangian coordinate for the same fluid element in following the hydrodynamics after the second pulse, etc. The Eulerian coordinate $\tilde{r}$, the position of the fluid element at time $\tilde{t}_n$, can be regarded as a function of $\tilde{r}_{n-1}$ and $\tilde{t}_n$. By definition,

$$\tilde{r}_n = \tilde{r}(\tilde{r}_{n-1},\ \tilde{t} = \tilde{\tau}_n). \tag{3.1}$$

We also define $\tilde{T}_{n-1}(\tilde{r})$, $\tilde{c}_{n-1}(\tilde{r})$, $\tilde{\rho}_{n-1}(\tilde{r})$, $\tilde{P}_{n-1}(\tilde{r})$ as the local (dimensionless) temperature, sound speed, density and pressure characterizing the channel at $\tilde{t}_n = 0^-$, just before the arrival of the n^{th} pulse, By assumption,

$$\tilde{P}_{n-1}(r) = \tilde{P}_{n-1} \ \text{(constant)}. \tag{3.2}$$

If the pulse spacing is long enough for the channel to come to rest in pressure balance,

$$\tilde{P}_n = 1 \ \text{ for all } n, \tag{3.3a}$$

and

$$\tilde{r}_n \equiv \tilde{r}(\tilde{r}_{n-1},\ \tilde{t}_n = \infty). \tag{3.3b}$$

For the special case of the first pulse, $n - 1 = 0$,

$$\tilde{T}_{n-1}(\tilde{r}) = \tilde{c}_{n-1}(r) = \tilde{\rho}_{n-1}(r) = 1. \tag{3.4}$$

The pressure at time ($\tilde{t}_n = 0^+$), just after the arrival of the n^{th} pulse, is taken to be

$$\tilde{P}(\tilde{r}_{n-1},\ \tilde{t}_n = 0^+) = \tilde{P}_{n-1}\left[1 + \frac{\tilde{P}_{on}}{(1 + \tilde{r}_{n-1})^2}\right]. \tag{3.5}$$

We have studied a wide variety of cases with hydrodynamic code simulations. Since our purpose here is to elucidate the principal features of the hydrodynamic evolution and arrive at scaling laws, rather than to overwhelm the reader with data, we show only the results of a few such simulations for a second pulse propagating in the channel formed by the first pulse, and arriving at a time when the channel is near its minimum density/pressure state.

B. Pulse-to-Pulse Evolution of Channel Density

We consider first the case in which pulse spacing is long enough so that the channel comes to rest in pressure balance with the ambient gas. Following exactly the same reasoning that led to Eqs. (2.10c), (2.12), but translating it into the notation just described, we find that the channel profile, when it comes to rest after n beam pulses, can be expressed in terms of the

profile after $n-1$ pulses by

$$\tilde{\rho}_n(\tilde{r}_{n-1}) = \tilde{\rho}_{n-1}(\tilde{r}_{n-1})\,[\tilde{P}_n(\tilde{r}_{n-1},\ \tilde{t}_n = 0^+)]^{-1/\gamma} \exp[-\Delta S_n(\tilde{r}_{n-1})/c_p]$$

$$= \tilde{\rho}_{n-1}(\tilde{r}_{n-1})\left[1 + \frac{\tilde{P}_{on}}{(1+\tilde{r}_{n-1}^2)^2}\right]^{-1/\gamma} \exp[-\Delta S_n(\tilde{r}_{n-1})/c_p], \tag{3.6}$$

$$\tilde{r}_n^2 = \int_o^{\tilde{r}_{n-1}^2} d(\tilde{r}_{n-1}')^2\, \frac{\tilde{\rho}_{n-1}(\tilde{r}_{n-1}')}{\tilde{\rho}_n(\tilde{r}_{n-1}')}. \tag{3.7}$$

We recall from Sec. 2 that $\exp[-\Delta S_n(\tilde{r}_{n-1})/c_\rho]$ represents a small (typically $< 20\%$) correction, due to the entropy increase $\Delta S_n(\tilde{r}_{n-1})$ when the outward propagating shock overruns the fluid element defined by Lagrangian coordinate $\tilde{r}_{n-1}$. To the accuracy required to calculate channel densities, we find that the heuristic formula for shock strength, Eq. (2.23), is also applicable to the present case of a pulse depositing energy in a pre-existing channel. This is evidently true because the shock evolution depends principally on the ratio of energy deposited as overpressure to energy density in the gas before the passage of the pulse; the latter is unchanged by the presence of the pre-existing channel, since we have assumed that the channel is at ambient pressure. Rewriting Eqs. (2.23,2.24), we have

$$\exp[-\Delta S_n/c_p] = \frac{\rho_n^-}{\rho_n^+}\left[\frac{6-\rho_n^-/\rho_n^+}{6\rho_n^-/\rho_n^+ - 1}\right]^{5/7}, \tag{3.8}$$

where the density jump at the shock is

$$\frac{\rho_n^-}{\rho_n^+}(r_o) \approx \begin{cases} 1, & \tilde{r}_{n-1} < 0.8 \\ 1 + 0.33\,\tilde{P}_{on}^{1/4}\,\tilde{r}_{n-1}, & 0.8 \leqslant \tilde{r}_{n-1} < 3 \\ 1 + 1.7\,\tilde{P}_{on}^{1/4}\,\tilde{r}_{n-1}^{-1/2}, & 3 \leqslant \tilde{r}_{n-1} \end{cases} \tag{3.9}$$

Eqs. (3.6-3.9) now give a complete description of the channel density profile, when pressure balance is restored after the passage of a pulse in a channel, in terms of the overpressure $\tilde{P}_{on}$ and the profile of the pre-existing channel. By iterating these equations n times, we obtain the channel profile after the passage of n pulses in initially uniform ambient gas.

As in the case of an initial pulse depositing its energy in uniform gas, we find that for all cases with central overpressure $\tilde{P}_{on} \gtrsim 1$, the pressure profile $\tilde{P}(\tilde{r}, \tilde{t}_n)$ reaches a very broad, shallow minimum value $\tilde{P}_m$, slightly less than unity, at sometime $\tilde{t}_{mn}$. This is shown for several fluid code runs in Figs. 3.4-3.6. In fact, the value of $\tilde{P}_m$ is found to depend only on $\tilde{P}_{on}$, and not on the channel properties, i.e., it is given by Fig. 2.13, even in the presence of a pre-existing channel. For practical purposes, it is sufficient to estimate $\tilde{P}_m = 0.88$ for all cases with $\tilde{P}_{on} \gtrsim 1$.

It might be desirable, in some cases, to choose the pulse spacing such that each fresh beam pulse arrives at the time $\tilde{t}_{mn}$ when the channel is deepest, rather than after it has returned to pressure balance. In this case, since $\tilde{P}(r) \approx \tilde{P}_m \approx 0.88$ is essentially constant over the channel (and the same for each successive pulse), Eqs. (3.6-3.9) remain formally unchanged for $n \geqslant 2$. We note, however, that the overpressure parameter $\tilde{P}_{on}$ which occurs in Eq. (3.6), is defined in Eq. (3.5) relative to the *channel* pressure $\tilde{P}_{n-1}$ at $t_n = 0$; thus, for a given amount of energy deposition by the n^{th} pulse, $\tilde{P}_{on}$ is larger if the channel is at minimum pressure rather than ambient pressure. The evolution following the first pulse begins with $\tilde{P}(r) = 1$ and ends with $\tilde{P}(r) \approx 0.88$, so for the first pulse Eq. (3.6) is modified to

$$\tilde{\rho}_1(\tilde{r}_o) = \left[1 + \frac{\tilde{P}_{o1}}{(1+\tilde{r}_o)^2}\right]^{-1/\gamma} (0.88)^{1/\gamma} \exp\left[-\Delta S(\tilde{r}_{n-1})/c_P\right], \tag{3.10}$$

as discussed in detail in Sec. 2C.

In practice, the dependence of the channel evolution on the exact pulse spacing is rather weak, and interpolation is easily performed, provided the channel pressure is anywhere close to the ambient pressure when the next pulse arrives.

C. Time Evolution

The time scales for radial expansion, following energy deposition by a beam pulse in a preformed channel, are analogous to those for energy deposition in uniform ambient gas, discussed in Sec. 2D. The situation is more complicated because the sound speed $c_{n-1}(r)$ in the pre-existing channel is now a function of r.

The time evolution of $\tilde{\rho}(\tilde{r}=0,\tilde{t}_n)$ and of the shock radius $\tilde{R}_s(\tilde{t}_n)$ are shown in Figs. 3.10 and 3.11, for three cases run on the fluid code. Once again, we note, in three figures and in Figs. 3.1-6, the existence of three stages of development. In the first stage, rapid expansion occurs over $\tilde{r} \lesssim 1$, initially at the sound speed $c(\tilde{r}=0,\ \tilde{t}_n=0^+)$ of the heated central region. Since the pre-existing channel is typically much broader then $\tilde{r}=1$, this stage samples only the uniform central region of the channel. Thus this stage of evolution is similar to that which occurs for energy deposition in uniform ambient gas, except that the ambient sound speed is replaced by the sound speed $c_{n-1}(r)$ in the pre-existing channel. Indeed we see in Fig. 3.10 that the *change* in density at $\tilde{r}=0$ is 90% completed when $\tilde{t}_n = 0.7\ \tilde{T}_{n-1}^{-1/2}$, in analogy with the conclusion of Sec. 2D for the first pulse.

In the second stage, a low Mach number shock propagates over the final channel radius, at a speed moderately higher than the *local* sound speed $c_{n-1}(\tilde{r})$ in the pre-existing channel. Since $c_{n-1}(\tilde{r})$ varies widely over the channel, the time scale for this process depends on both the strength of the n^{th} pulse and the depth and width of the pre-existing channel, making it difficult to give any simple, general formula for this time scale. In general, a minimum pressure is reached, which is nearly constant over a broad region, and this occurs at a time t_{mn} which varies from

$$\tilde{t}_{mn} \approx (1\ to\ 2) \times (\tilde{P}_{on}+1)^{1/2}$$

for a pulse which is strong enough to significantly broaden the channel to

$$\tilde{t}_{mn} \approx 1.2 \times (\tilde{P}_{on} + 1)^{1/2}\, \tilde{T}_{n-1}^{-1/2} \quad (\tilde{r} = 0)$$

for a pulse which is too weak to produce much channel broadening. However, the minimum pressure itself depends essentially only on $\tilde{P}_{on}$, and not on the channel properties, and is given to good accuracy by Fig. 2.13; for the whole range $\tilde{P}_{on} \geqslant 1$, this minimum pressure is

$$\tilde{P}_{nm} \sim 0.85 \text{ to } 0.9.$$

In the third stage, the channel slowly returns to pressure equilibrium at $\tilde{P}(\tilde{r}) = 1$. As in the case of a first pulse into ambient gas, this is essentially a linear sound wave propagation process, and the e-folding time for the approach to equilibrium is typically about $1.5\tilde{t}_{mn}$.

IV. WEAK BEAM PULSE — LINEARIZED HYDRODYNAMICS

In this report we have studied the nonlinear hydrodynamic response to a beam pulse which instantaneously heats the gas it traverses. If the pulse happens to be weak, i.e., the overpressure is much smaller than the ambient pressure P_A, and the air is initially uniform, then the hydrodynamics can be linearized and solved analytically. Such calculations are of direct interest in application to a weak pulse or a series of weak pulses, and in addition provide valuable insight into the hydrodynamic features of the general problem. Results of this type have been presented by Fader[11] for the special case of a Gaussian radial heating profile. We extend these results somewhat here, and treat in addition the cases of Bennett and step function heating profiles.

In the notation of this section, ambient quantities, e.g. pressure P_A, density ρ_A, sound speed c_A, temperature T_A, are designated by subscript A. Perturbed quantities are defined $\Delta P(r,t)$, $\Delta\rho(r,t)$, $\Delta c(r,t)$, $\Delta T(r,t)$, and fluid radial velocity $\Delta u(r)$ and are all assumed to be small, of first order. The problem becomes essentially one of linear sound propagation driven

by a given initial overpressure. Weak shock waves do, strictly speaking, eventually form, but this occurs at a very late time, and any accompanying entropy increases are higher order, and thus negligible. Thus the isentropic solution of Eqs. (2.10c), (2.12) for the density profile holds at late times (when pressure balance is restored). Furthermore, these equations reduce to the very simple, linearized form

$$\Delta\rho(r,t=\infty) = -\rho_A \frac{\Delta P(r,0^+)}{\gamma P_A} = -\frac{\Delta P(r,0^+)}{c_A^2}, \tag{4.1}$$

$$\Delta T(r,t=\infty) = \frac{\Delta T(r,0^+)}{\gamma}. \tag{4.2}$$

The late-time density and temperature profiles have exactly the shape and width of the initial overpressure profile. We see from Eq. (4.2) that a fraction γ^{-1} of the inital overpressure thermal energy remains in the channel when it comes to rest. The remainder of this energy is carried to $r = \infty$ by an outward propagating acoustic pulse.

The time dependent hydrodynamic process is determined by the linearized fluid equations,

$$\frac{\partial\Delta\rho}{\partial t} + \frac{\rho_A}{r}\frac{\partial}{\partial r}(r\Delta u) = 0, \tag{4.3}$$

$$\frac{\partial\Delta u}{\partial t} = -\frac{1}{\rho_A}\frac{\partial\Delta P}{\partial r}, \tag{4.4}$$

with the linearized adiabatic equation of state

$$\frac{dP}{d\rho} = \frac{\Delta P(r,t) - \Delta P(r,0)}{\Delta\rho(r,t)} = c_A^2, \tag{4.5a}$$

$$\Delta T(r,t) = \frac{\Delta T(r,o)}{\gamma} + \left[1 - \frac{1}{\gamma}\right]\frac{\Delta P(r,t)}{\rho_A}, \tag{4.5b}$$

and the initial conditions

$$\Delta\rho = 0, \quad \Delta P(r,0) \text{ given.}$$

It is convenient to define a velocity potential $\phi(r,t)$ by

$$u(r,t) = \frac{\partial \phi}{\partial t}.$$

Equations (4.3)-(4.6) then reduce to the linear sound wave equation

$$\frac{1}{r}\frac{\partial}{\partial r} r \frac{\partial \phi}{\partial r} = \frac{1}{c_A^2}\frac{\partial^2 \phi}{\partial t^2}, \tag{4.8}$$

with initial conditions

$$\phi(r,0) = 0, \tag{4.9}$$

$$\frac{\partial \phi}{\partial t}(r,0) = -\frac{P(r,0)}{\rho_0}, \tag{4.10}$$

and boundary conditions

$$\frac{\partial \phi}{\partial t}(0,t) = \phi(\infty,t) = 0. \tag{4.11}$$

Taking the Laplace transform in time, and the Fourier-Bessel transform,

$$\Delta P_k(t) \equiv \int_o^\infty dr r\, J_o(kr)\, \Delta P(r,t) \tag{4.12}$$

in space, Eqs. (4.8)-(4.10) reduce to

$$\phi_{k,s} = -\frac{1}{P_A}\frac{\Delta P_k(t=0)}{k^2 c_A^2 + s^2}, \tag{4.13}$$

where s is the Laplace transform variable. The Laplace-Mellin inverson of (4.13) is easily done, giving

$$\phi_k(t) = -\frac{\Delta P_k(t=0)}{kc_A\rho_A}\sin(kc_A t). \tag{4 14}$$

Applying the inverse Fourier-Bessel transform yields the solution,

$$\phi(r,t) = -\frac{1}{c_A\rho_A}\int_0^\infty dk \sin(kc_A t)\, J_o(kr)\, \Delta P_k(t=0). \tag{4.15a}$$

$$= -(c_A\rho_A)^{-1}\int_0^\infty dr' r' \Delta P(r',t=0)\int_0^\infty dk \sin(kc_A t)\, J_o(kr) J_o(kr'). \tag{4.15b}$$

We note that the k-integration in (4.15b) can be performed in closed form, thus reducing the solution to a single quadrature. However we take a different route. For computational purposes, it is convenient to use the relation

$$J_o(kr) = \frac{2}{\pi} \int_r^\infty dx \, \sin(kx) \, (x^2 - r^2)^{-1/2} \tag{4.16}$$

to recast Eq. (4.15a) in the form

$$\phi(r, t) = -(\pi c_A \rho_A) \int_r^\infty dx (x^2 - r^2)^{-1/2}$$

$$\times \int_o^\infty dk \, \{\cos[k(ct - x)] - \cos[k(ct + x)]\} \, \Delta P_k(0). \tag{4.17}$$

The k-integration in (4.17) can be peformed analytically for many choices of $\Delta P(r, 0)$.

Next we consider three particular choices of $\Delta P(r, 0)$: the Bennett profiie,

$$\Delta P(r_o) = \frac{\Delta P_o}{1 + r^2/a^2)^2}, \tag{4.18a}$$

for which (with K_1 the modified Hankel function),

$$\Delta P_k(0) = \frac{1}{2} \, a^3 k \, \Delta P_o \, K_1(ka); \tag{4.18b}$$

the step function,

$$\Delta P(r, 0) = \Delta P_o \, H(a - r) \equiv \begin{cases} \Delta P, & r \leqslant a \\ 0, & r > a \end{cases} \tag{4.19a}$$

for which

$$\Delta P_k(0) = \frac{a}{k} \, \Delta P_o \, J_1(ka); \tag{4.19b}$$

and the Gaussian profiie,

$$\Delta P(r, 0) = \Delta P_o \exp(-r^2/a^2), \tag{4.20a}$$

for which

$$\Delta P_k(0) = \frac{1}{8} a^2 \exp\left[-\frac{1}{4} \, k^2 a^2\right]. \tag{4.20b}$$

In all three cases, the k-integration in Eq. (4.17) can be performed explicitly, giving the following results for ϕ in terms of single quadratures (using a further transformation, $x = r \cosh z$ to remove the logarithmic singularity at $r = x$). For a Bennett profile,

$$\phi(r,\ t) = -\frac{\Delta P_o a^4}{4\rho_A c_A} \int_o^\infty dz \left\{ \left[(c_A t - r\ \mathrm{cosh}z)^2 + a^2 \right]^{-3/2} - \left[(c_A t + r\ \mathrm{cosh}z)^2 + a^2 \right]^{-3/2} \right\}; \tag{4.21}$$

for a step function profile

$$\phi(r,\ t) = -\frac{\Delta P_o a}{\pi \rho_A c_A} \int_o^\infty dz \left\{ \left[1 - \left(\frac{c_A t - r\ \mathrm{cosh}z}{a} \right)^2 \right]^{\frac{1}{2}} \times H(a - |c_A t - r\ \mathrm{cosh}z|) - \left[1 - \left(\frac{c_A t + r\ \mathrm{cosh}z}{a} \right)^2 \right]^{\frac{1}{2}} H(a - |c_A t + r\ \mathrm{cosh}z|) \right\}; \tag{4.22}$$

and for Gaussian profile,

$$\phi(r,\ t) = \frac{-\Delta P_o a}{2\rho_A c_A \pi^{1/2}} \int_o^\infty dz \left\{ \exp\left[-\left(\frac{ct - r\ \mathrm{cosh}z}{a} \right)^2 \right] - \exp\left[-\left(\frac{ct + r\ \mathrm{cosh}z}{a} \right)^2 \right] \right\}. \tag{4.23}$$

The single integrals in Eqs. (4.21)-(4.23) have been carried out numerically. The quantities $\Delta P(r,t)$, $\Delta\rho(r,\ t)$, $\Delta T(r,t)$ are determined from $\phi(r,t)$ via Eqs. (4.5). The results, in each case, are universal when expressed in terms of the dimensionless variables $\tilde{r} = r/a$, $\tilde{t} = c_A t/a$, $\tilde{P}' = \Delta P/P_A$, $\tilde{\rho}' = \tilde{\Delta}\rho/\rho_A$, $T' = \Delta T/T_A$. In Figs. 4.1 through 4.5 we show profiles of $\Delta\rho(r)$ and $\Delta P(r)$ at a sequence of times, for the Bennett and step function profiles, and in Figs. 4.5 and 4.6 the time dependence of $\rho(r = 0)$ is displayed.

In each case an outward propagating sound pulse, and an inward propagating rarefacton wave, originate at the point of maximal $|\partial P(r, o)/\partial r|$, both propagating at c_A. This is particularly clear for the step function initial profile, for which there is no disturbance at a point r until $t > |a - r|/c_A$. The outward pulse propagates to $r = \infty$, carrying with it a constant fraction $(1 - \gamma^{-1})$ of the energy deposited in the medium. The density and pressure at points near the axis drops monotonically until the time $\tilde{t}_m$ when the rarefaction pulse hits the axis. At this time, the pressure on axis reaches a minimum $P_m(r = 0)$ and then rebounds slowly and monotonically until it reaches P_A. There is no perceptible series of oscillations or "bounces" of the channel that is left behind. The value of the density minimum, $\rho_m(r = 0) = \rho(r = 0, \tilde{t} = \tilde{t}_m)$, is given in Table 4 for each of the three assumed profiles of $P(r_o)$, step function, Gaussian, and Bennett.

All of these features carry over, with obvious modification, to the nonlinear hydrodynamics studies in Sec. 2. However one difference is that in the nonlinear case, with $\Delta P(0, 0) \gtrsim P_A$, we found that at time t_{nm} the pressure is practically constant, at its minimum value, over the reduced-density channel. In the present linear regime, the pressure wave of course has the same characteristic wavelength as the density wave; thus the pressure profile at t_m is no broader than the density channel, and different parts of the channel reach minimum pressure at different times.

V. CONCLUSIONS

In this report, we have studied the hydrodynamics of channel formation over a wide range of parameters ranging from very weak overpressures up to overpressures ~40 times ambient. Channel cooling and variation of the adiabatic index γ with ρ and T have been omitted. The main conclusions, for the case of heating pulses with smooth (Bennett) radial profiles, are as follows.

(i) The density reduction at the center of the channel, when the channel motion comes to rest, is easily and accurately calculated by the isentropic model, for any number of widely spaced pulses. Results are given in Table 3 and Eq. (2.12).

(ii) The isentropic model of Table 3 and Eqs. (2.10c), (2.12) is accurate to within $\lesssim$ 20% per pulse in calculating the overall shape and width of the channel, for overpressure $\tilde{P}_o \lesssim$ 40 (it is more accurate for smaller overpressures).

(iii) An adiabatic model, extended to include shock wave heating, is highly accurate in calculating overall channel shape and width. Results are given in Table 3 and Eqs. (2.8, 10c, 23, 24), (3.6-9).

(iv) During the hydrodynamic evolution, the channel undershoots its final density by a factor $\sim$10%, essentially constant over the channel, and practically independent of $\tilde{P}_o$ for $\tilde{P}_o \gtrsim 1$. It then returns slowly to pressure balance, without "ringing".

(v) The time scales for channel formation near $r = 0$, for the whole channel to reach minimum density, and for the return to pressure equilibrium, are distinct, and are given in Table 2. The first time scale is typically up to an order of magnitude shorter than the other two.

(vi) For very weak beam pulses, the complete time-dependent linearized hydrodynamics can be solved, in terms of quadratures. Results are given in Sec. 4.

(vii) The self-similar blast wave theories of classical hydrodynamic lore[5] are only applicable to beam heating much stronger than are considered here.

ACKNOWLEDGMENTS

The authors gratefully acknowledge the use of computer code modules written by Dr. J. Boris, and assistance from Dr. Boris, Dr. M. Fritts, and Dr. D. Colombant on numerical techniques. This research was supported by Naval Surface Weapons Center.

REFERENCES

01. R. J. Briggs, T. C. Clark, T. J. Fessenden, R. E. Hester, and E. J. Lauer, *Proceedings of 2 nd International Conference on High Power Electron and Ion Beam Research and Technology*, October 1977, Vol. I, p. 319.

02. D. Koopman, J. R. Greig, R. Pechacek, A. Ali, I. M. Vitkovitsky, and R. Fensler, *Proceedings of the XIVth International Conference Phenomena in Ionized Gases*, Grenoble, France, July 1979, p. C7-419.

03. J. R. Vaill, D. A. Tidman, T. D. Wilkerson, and D. W. Koopman, Appl. Phys. Lett. **17**, 20 (1970).

04. P. A. Miller, L. Baker, J. R. Freeman, L. P. Mix, J. W. Ponkey, and T. P. Wright, *Proceedings of 2nd International Topical Conference on High Power Electron and Ion Beam Research and Technology*, October 1977, Vol. I, p. 393.

05. L. D. Landau and F. M. Lifshitz, Fluid Mechanic, Addison-Wesley, Reading, Massachusetts, 1966, p.393.

06. E. P. Lee, Phys. Fluid, **19**, 60 (1976)

07. J. P. Boris, Computer Phys. Comm. **12** 67 (1976); NRL Memo Rept., 3237 (March, 1976)

08. D. G. Colombant and J. H. Gardner, J. Comp. Phys. **22**, 389 (1976)

09. M. S. Plesset, J. Appl. Phys. **25** 96 (1954); W. G. Penney and A. T. Price, *The Gas Globe* (Office of Naval Research, 1950), V.II, p. 145; G. I. Taylor and R. M Devies, loc. cit. p. 227

10. L. D. Landau and E. M. Lifshitz. loc. cit. p. 370

11. W. J. Fader, J. App. Phys **47**, 1975 (1976)

Table 1 — Notation

a	Typical (Bennett) radius of beam and of beam-heated region
c_p	Specific heat at constant pressure
c_v	Specific heat at constant volume
γ	$\equiv c_p/c_v$, adiabatic index, taken to be $\frac{7}{5}$
$P(r, t)$	Pressure
$\rho(r, t)$	Density
$T(r, t)$	Temperature
$c(r, t)$	Sound speed
P_A	Ambient pressure
ρ_A	Ambient density
T_A	Ambient temperature
c_A	Ambient sound speed
r	Position coordinate (Eulerian)
t	Time, measured since arrival of first beam pulse
t_n	Time, measured since the nth beam pulse ($t_1 \equiv t$)
τ_n	Time of arrival of nth pulse. $\tau_1 = 0$.
r_0	Initial position of a fluid element, used as a Lagrangian coordinate, i.e. a label for that element
r_{n-1}	Position of a fluid element at $t = \tau_n$, arrival time of nth pulse. Also used as a Lagrangian coordinate
$P_{n-1}(r)$	Pressure at time $t = \tau_n^-$
$\rho_{n-1}(r)$	Density at time $t = \tau_n$
$T_{n-1}(r)$	Temperature at time $t = \tau_n$
$C_{n-1}(r)$	Sound speed at time $t = \tau_n$
$P_n(r)$	Overpressue due to energy deposition by nth pulse
$\tilde{P}_{on}$	$P_n(r=o)/P_{n-1}$, used to label strength of nth pulse
r_{s0}	Lagrangian coordinate of fluid element where shock forms
t_s	Time when shock forms
$R_s(t)$	Shock location at time t
t_m	Time when channel reaches minimum pressure
$\Delta S(r_{0})$	Entropy increase, due to shock
$\tilde{P} \equiv P/P_A$	Dimensionless forms are defined similarly
$\tilde{\rho} \equiv \rho/\rho_A$	for various subscripted forms
$\tilde{T} \equiv T/T_A$	of P, ρ, T, c, r and t
$\tilde{c} \equiv c/c_A$	
$\tilde{r} \equiv r/a$	
$\tilde{t} \equiv c_A t/a$	

Table 2 — Time Scale for Hydrodynamics

1) Density reduction at $r = 0$. $\rho(r = 0)$ reduced 90% of the way to its asymptotic value, i.e. $\rho(0, \tilde{t}_n) = \rho(0, \infty) + 0.1\,[\rho_{n-1}(0) - \rho(0, \infty)]$	$\tilde{t}_n = 0.7\,[\tilde{T}_{n-1}(0)]^{-1/2}$
2) Minimum density and pressure, entire channel $\tilde{t}_n = \tilde{t}_{mn}$	
First pulse Strong pulse in existing channel Weak pulse in existing channel	$\tilde{t}_{m1} = 1.2(1 + \tilde{P}_o)^{1/2}$ $\tilde{t}_{mn} \approx$ (1 to 2) $(1 + \tilde{P}_o)^{1/2}$ $\tilde{t}_{mn} \approx 1.2\,(1 + \tilde{P}_o)^{1/2}\,[\tilde{T}_{n-1}(0)]^{1/2}$
3) Channel reaches pressure balance with ambient gas	$\tilde{t}_n \approx 3\tilde{t}_{mn}$

Table 3 — Channel Density After Gas Reaches Pressure Balance

(1) Channel density at $r = 0$

$$\rho_n(0) = \rho_{n-1}(0)\,(1 + \tilde{P}_{on})^{-1/\gamma} \text{ (Isentropic expansion)}$$

(2) Channel density profile

We label an element of gas by its position $\tilde{r}_{n-1}$ before the n^{th} pulse arrives. $\tilde{r}_n$ is the position of the same gas element after pressure balance is re-established.

$$\tilde{r}_n^2 = \int_o^{\tilde{r}_{n-1}^2} d(\tilde{r}_{n-1}')^2\,\frac{\tilde{\rho}_{n-1}(\tilde{r}_{n-1}')}{\tilde{\rho}_n(\tilde{r}_{n-1})},$$

$$\frac{\rho_n(\tilde{r}_{n-1})}{\rho_{n-1}(\tilde{r}_{n-1})} = \left[1 + \frac{\tilde{P}_{on}}{(1 + \tilde{r}_{n-1}^2)^2}\right]^{-1/\gamma} \exp[-\Delta S_n\,(r_{n-1})/c_p],$$

$$\exp[-\Delta S_n\,(r_{n-1})/c_p] = \frac{\rho^-}{\rho^+}\left[\frac{6 - \rho^-/\rho^+}{6\rho^-/\rho^+ - 1}\right]^{5/7} \text{ (entropy jump due to shock).}$$

$$\frac{\rho_-}{\rho_+}(r_{n-1}) = \begin{cases} 1, & \tilde{r}_o < 0.8 \\ 1 + 0.33\,\tilde{P}_{on}^{1/4}\,\tilde{r}_o, & 0.8 < \tilde{r} < 3 \\ 1 + 1.7\,\tilde{P}_{on}^{1/4}\,\tilde{r}_o^{-1/2}, & 3 < \tilde{r}_o \end{cases} \text{(density jump at shock).}$$

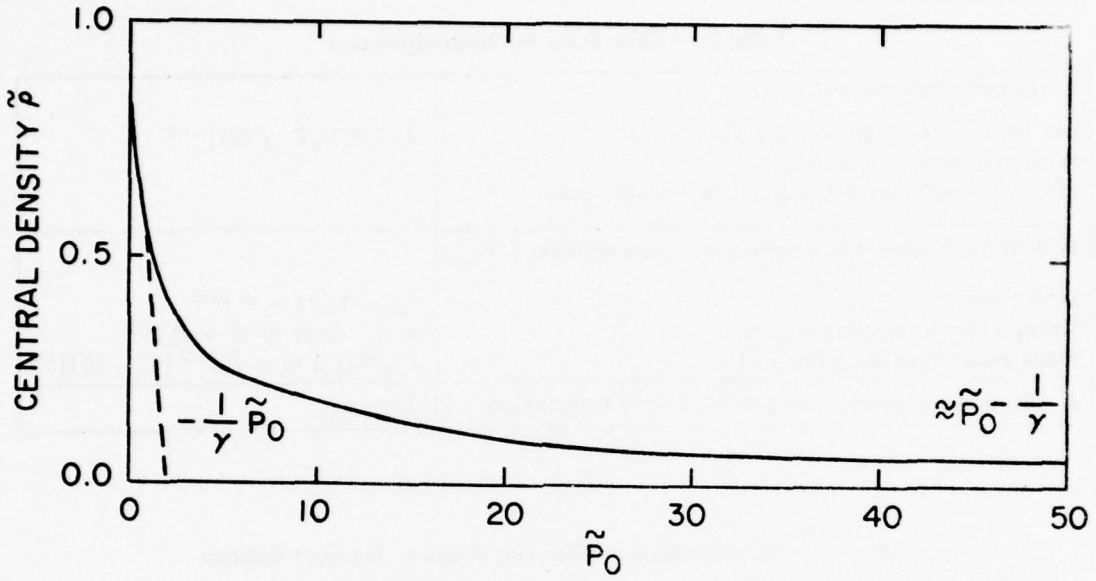


Fig. 1.1 — Final value of central density as a function of initial overpressure $\tilde{P}_0$ at $\tilde{r} = 0$, as given by the isentropic model.

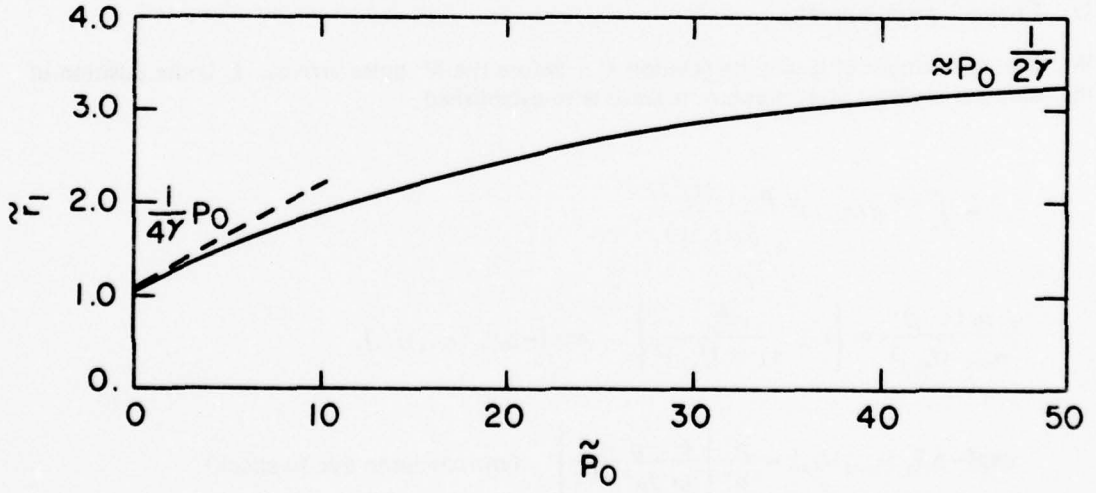


Fig. 1.2 — Final coordinate $\tilde{r}_1 \equiv r_1/a$ of a fluid element whose initial coordinate is $\tilde{r}_0 \equiv r_0/a = 1$, as a function of initial central overpressure $\tilde{P}_0$.

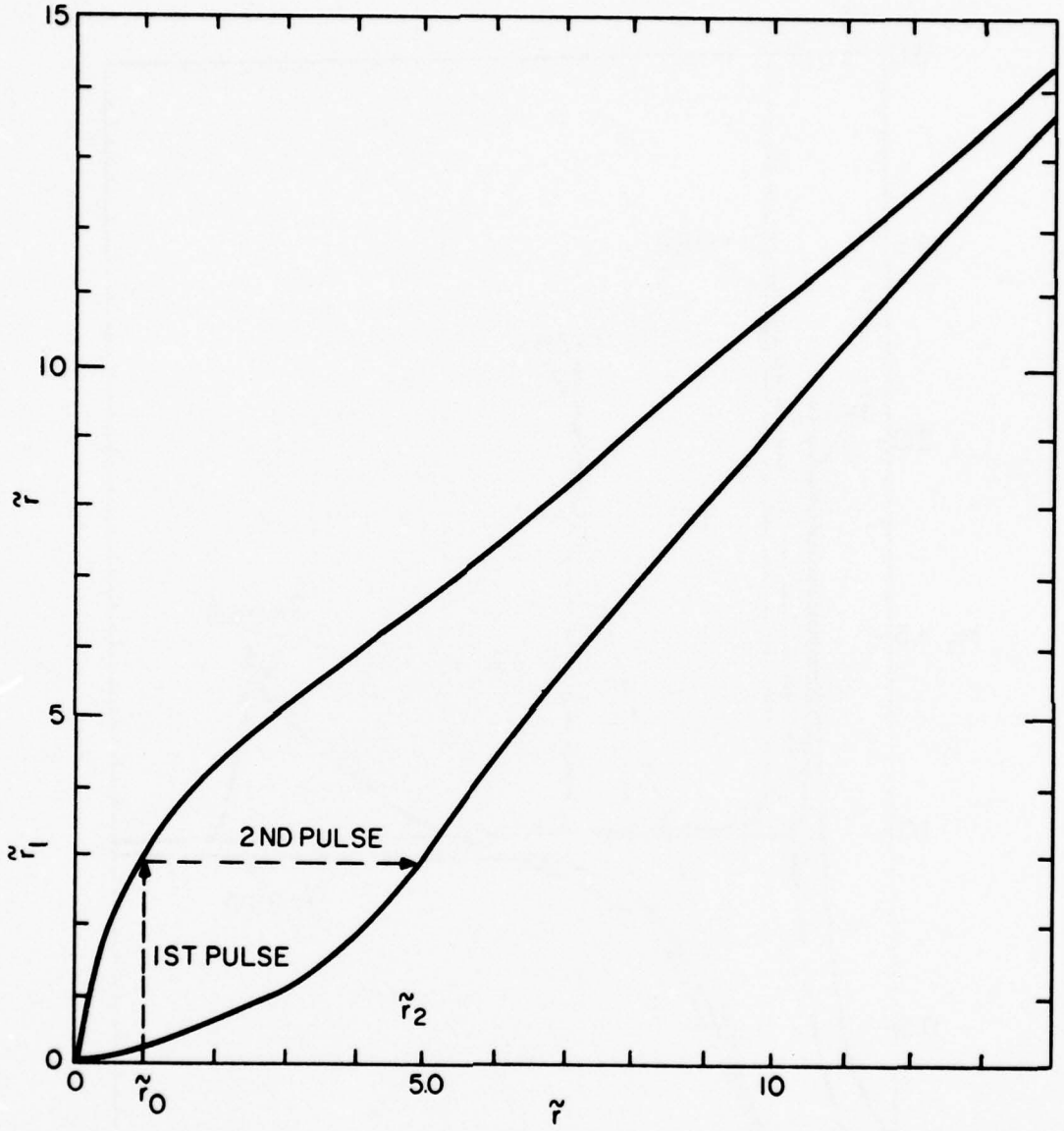


Fig. 1.3 — A graphical iterative method of going from the initial (dimensionless) coordinate $\tilde{r}_0$ of a fluid element, to the coordinate $\tilde{r}_1$ when the channel has returned to pressure equilibrium after the first pulse, to the value $\tilde{r}_2$ at pressure equilibrium after the second pulse, etc. For the case shown, $\tilde{P}_{01} = 4.32$, $\tilde{P}_{02} = 34.9$, and $\tilde{r}_0 = 1$.

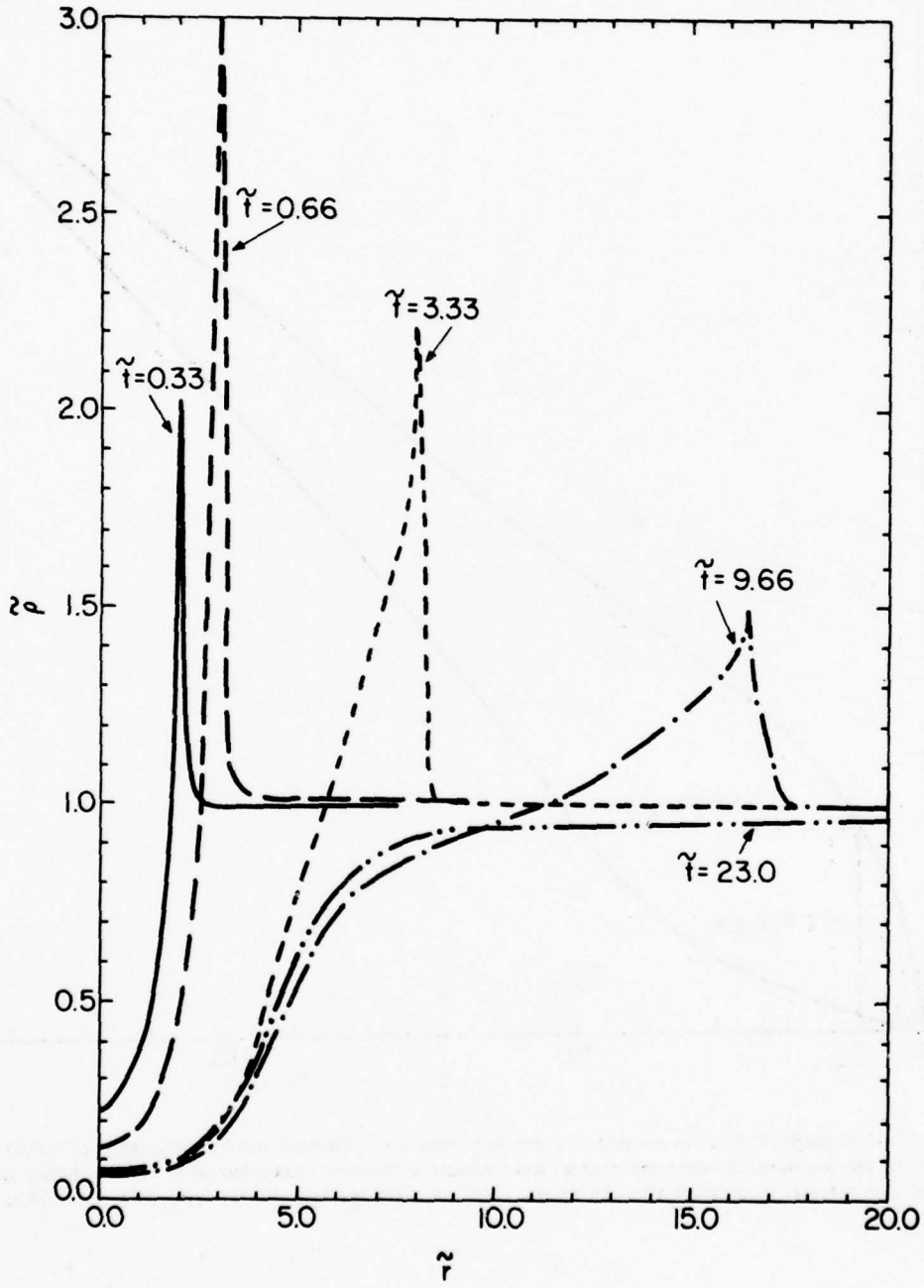


Fig. 2.1 — Radial profiles of the scaled density ($\tilde{\rho} \equiv \rho/\rho_4$) disturbance, for a Bennett initial pressure distribution (of radius a) with initial overpressure $\tilde{P}_0 \equiv P_0/P_4 = 4.20$ at $\tilde{r} \equiv r/a = 09$. Subscript A denotes ambient values. The times $\tilde{t} \equiv tc_4/a = 0.33$, 0.66, and 9.66, respectively, are close to the shock onset time, the time when the shock is strongest and a time when the channel density is close to but slightly below its final equilibrium.

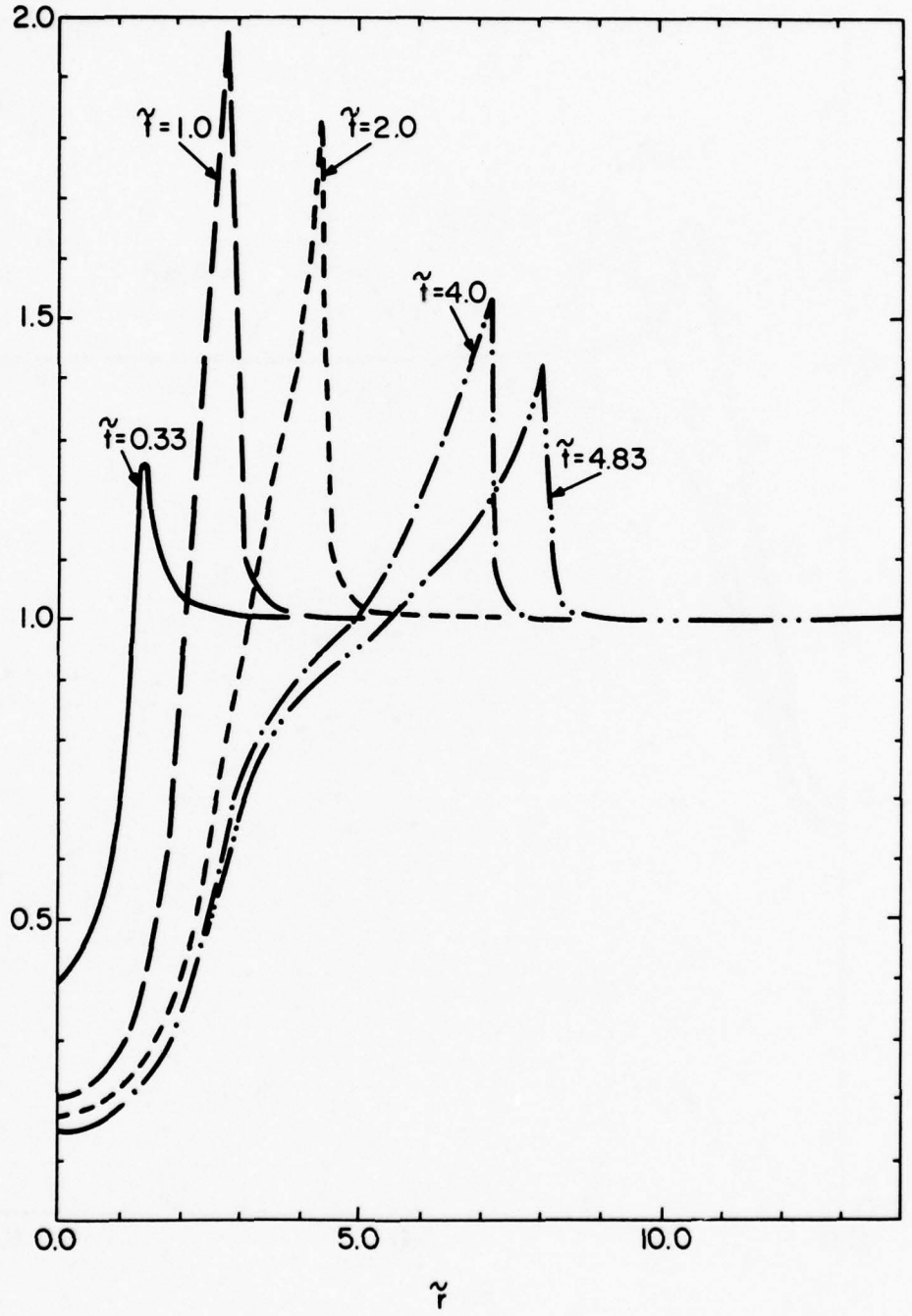


Fig. 2.2 — Radial profiles of the scaled density $\tilde{\rho}$, for a Bennett initial pressure distribution with initial overpressure $\tilde{P}_0 = 10.5$ at $\tilde{r} = 0$. Times are chosen by analogy to those in Fig. 2.1.

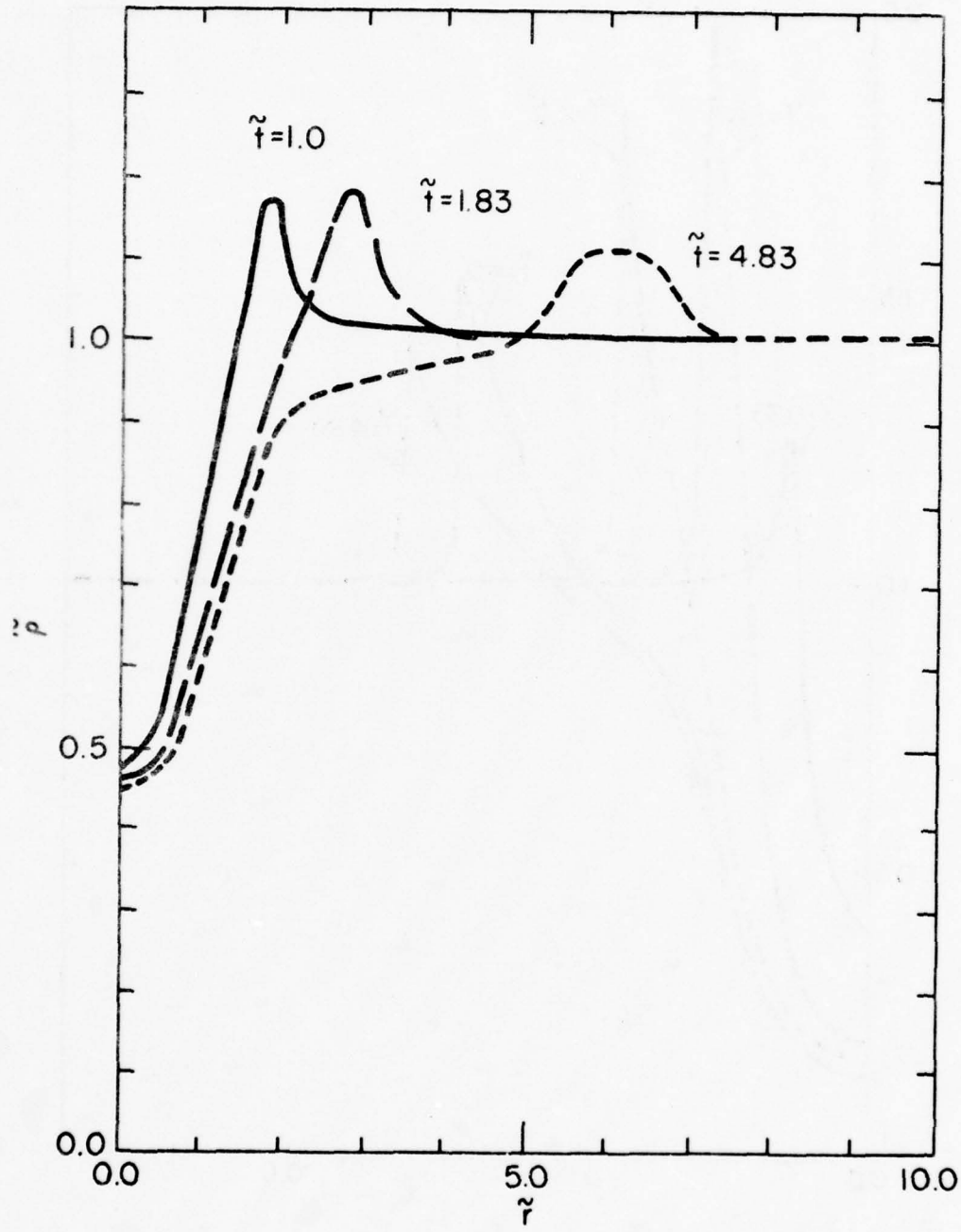


Fig. 2.3 — Radial profiles of the scaled density $\tilde{\rho}$, for a Bennett initial pressure distribution with initial overpresure $\tilde{P}_0 = 1.8$ at $\tilde{r} = 0$.

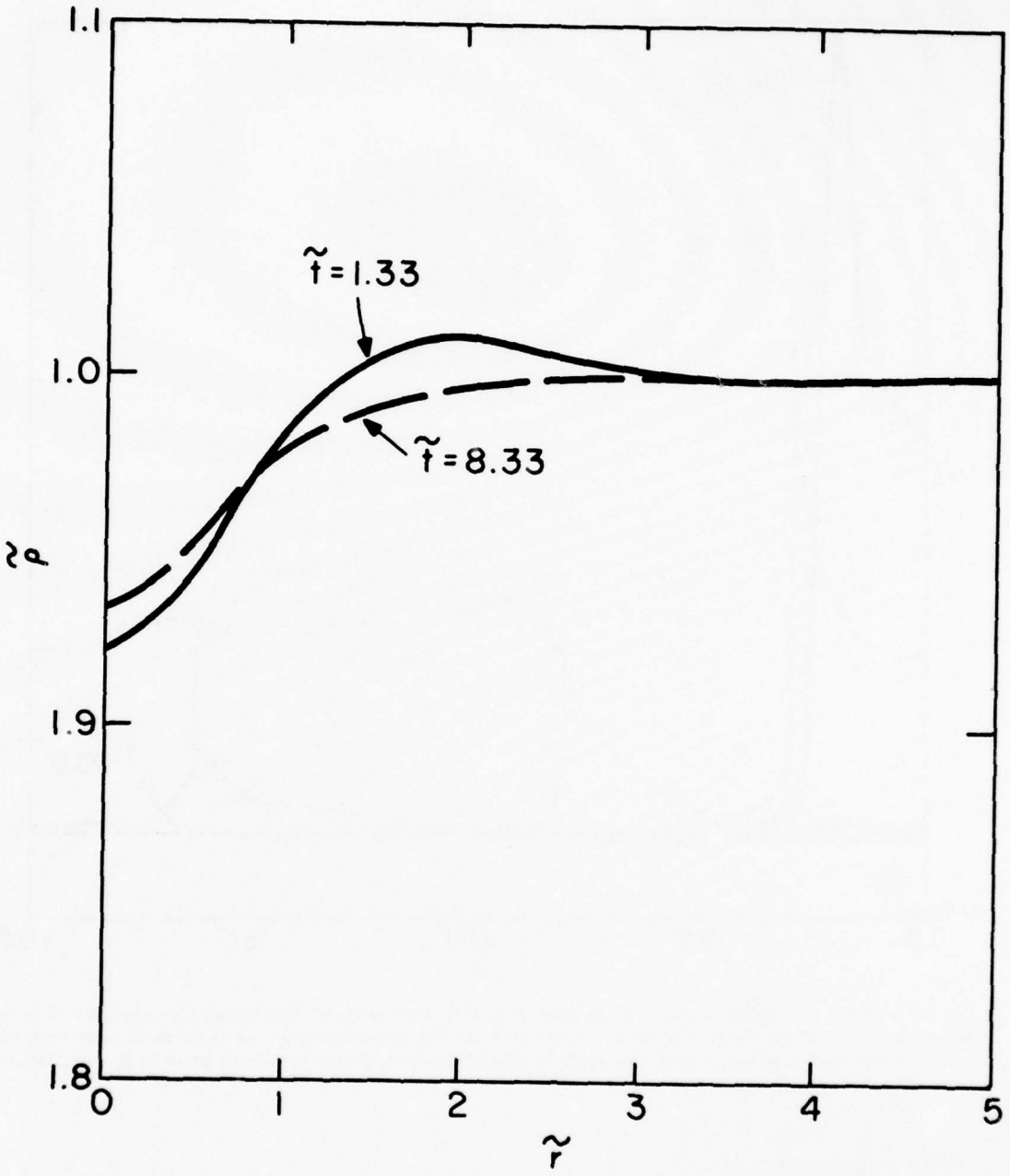


Fig. 2.4 — Radial profiles of scaled density $\tilde{\rho}$, for a Bennett initial pressure distribution with initial overpressure $\tilde{P}_0 = 0.1$ at $\tilde{r} = 0$.

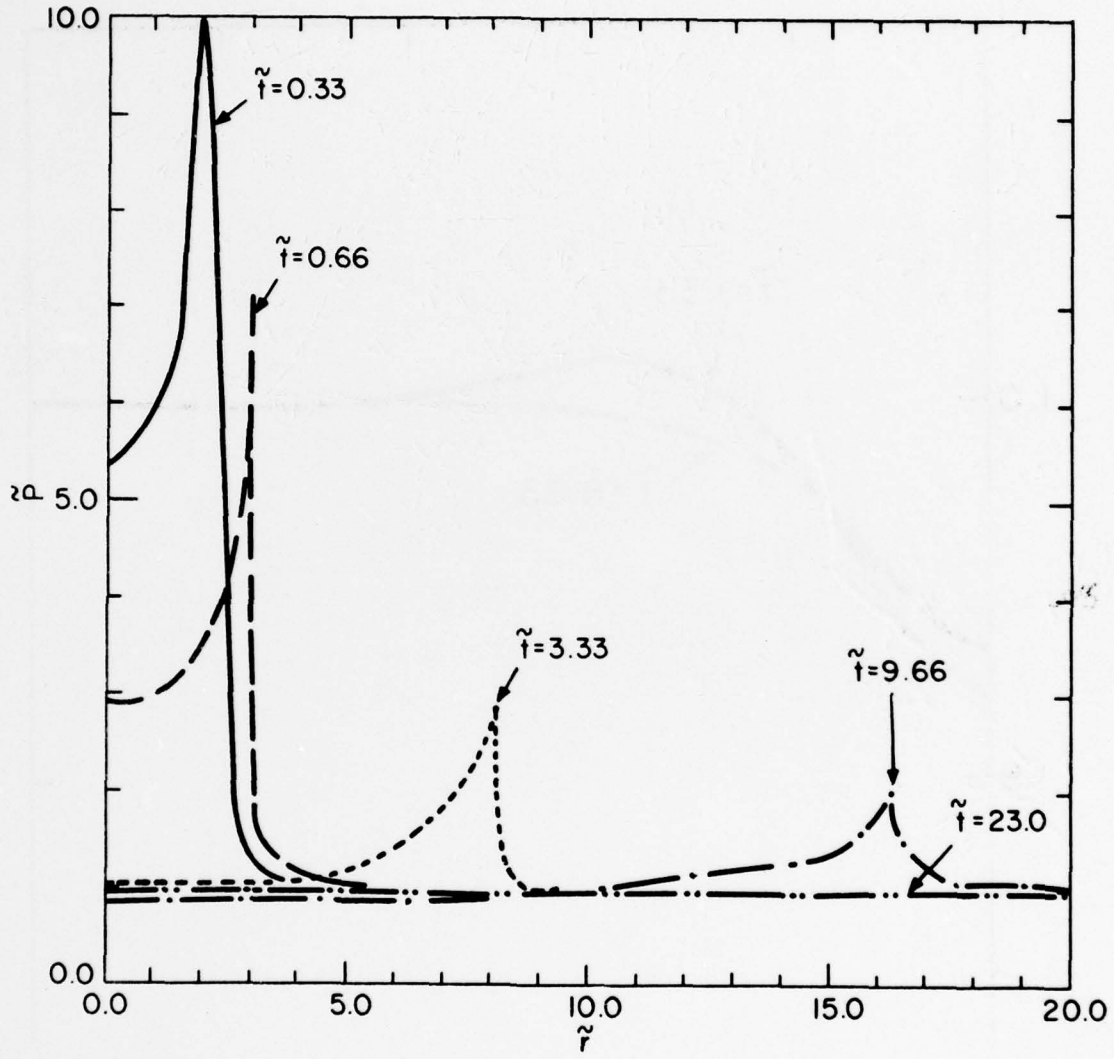


Fig. 2.5 — Radial distribution of the scaled pressure $\tilde{P} \equiv P/P_t$, for a Bennett initial pressure distribution with initial overpressure $\tilde{P}_0 = 42.0$ at $\tilde{r} = 0$. The times $t = 0.33$, 0.66 and 9.66 respectively are close to the shock onset time, the time when the shock is strongest and a time when the channel density is close to but slightly below its final equilibrium.

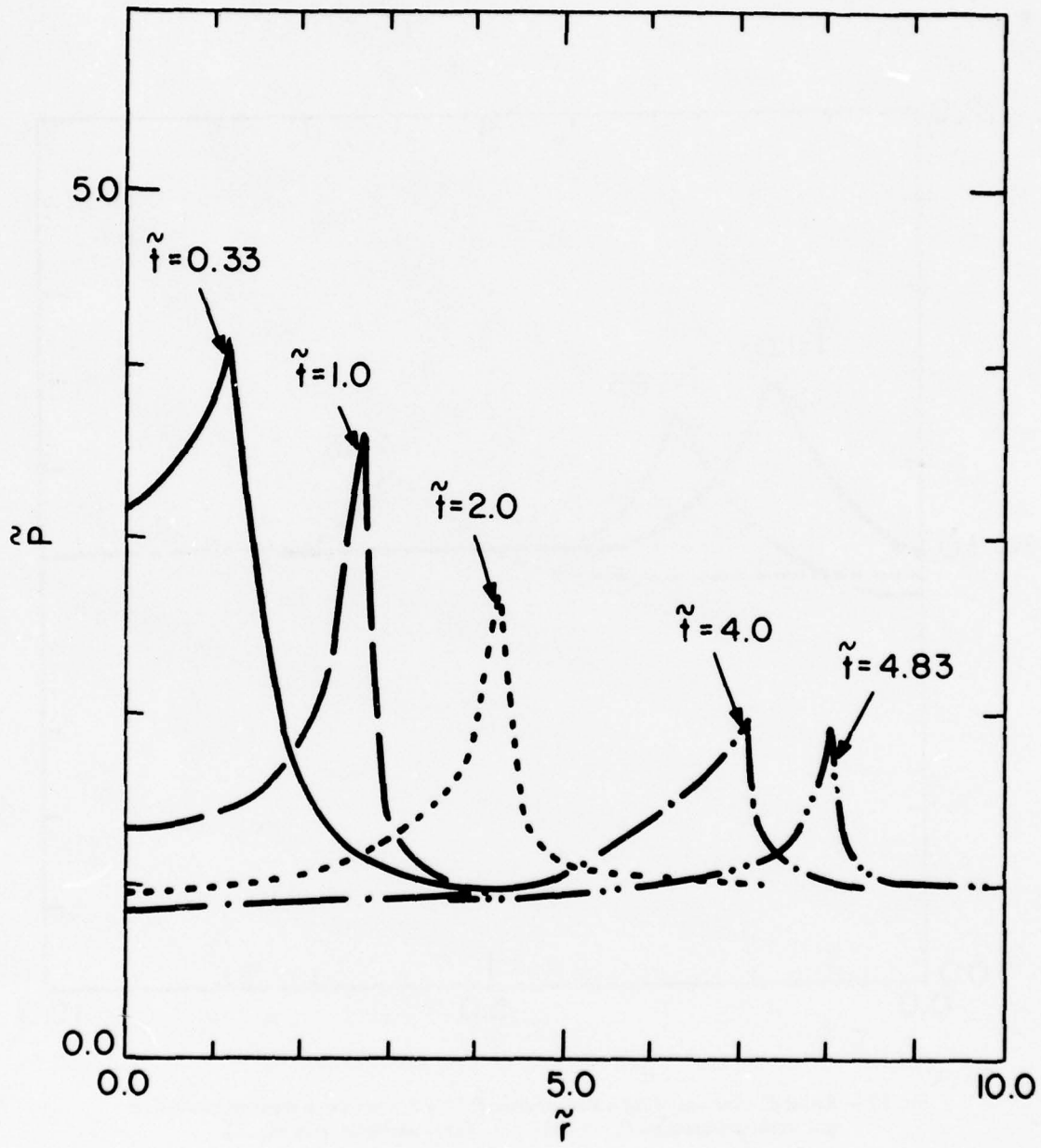


Fig. 2.6 — Radial distribution of the scaled pressure $\tilde{P}$, for a Bennett initial pressure distribution with initial overpressure $\tilde{P}_0 = 10.5$ at $\tilde{r} = 0$. Times are chosen by analogy to those in Fig. 2.5.

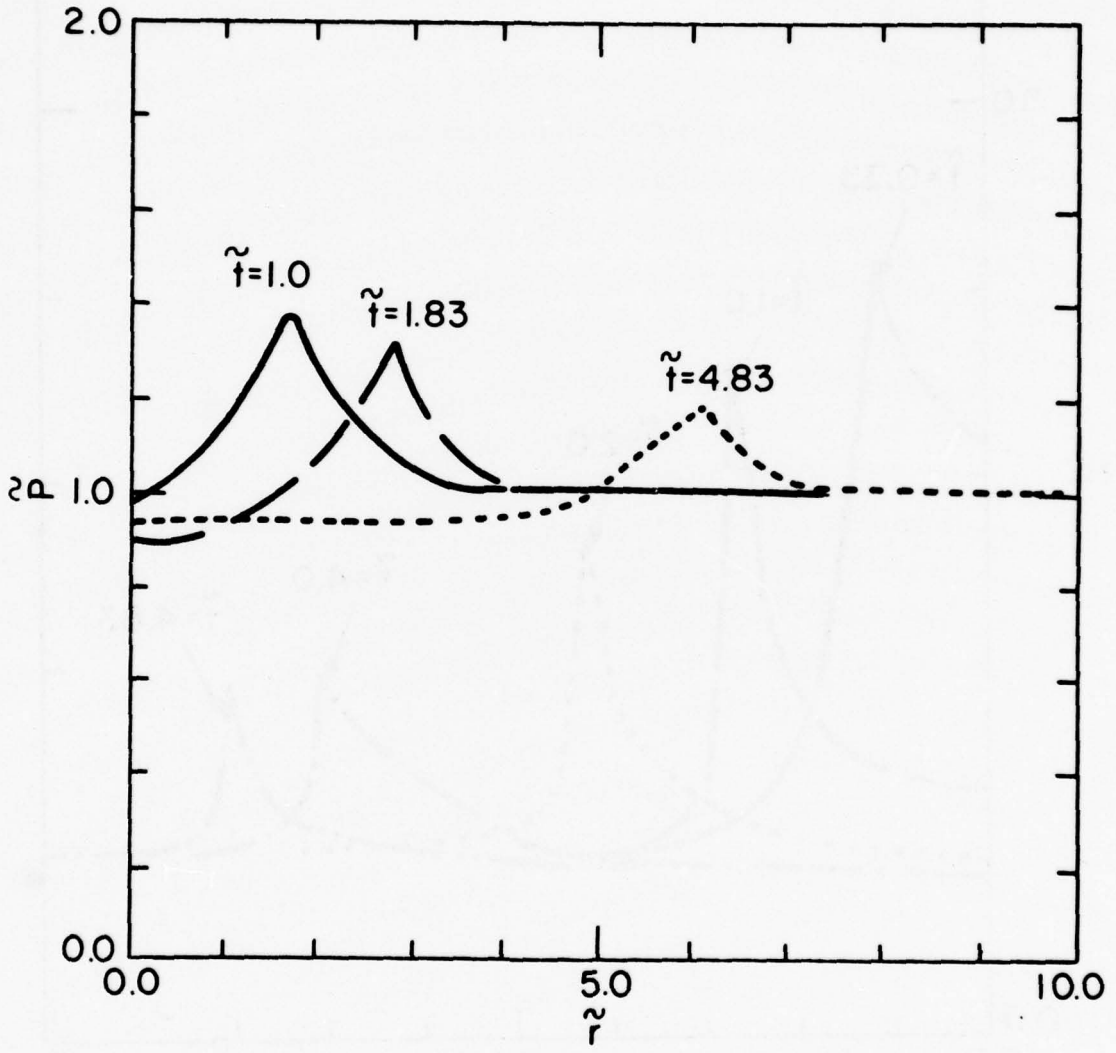


Fig. 2.7 — Radial distributions of the scaled pressure $\tilde{P}$, for a Bennett initial pressure distribution with initial overpressure $\tilde{P}_0 = 1.8$ at $\tilde{r} = 0$. Times are the same as Fig. 2.3.

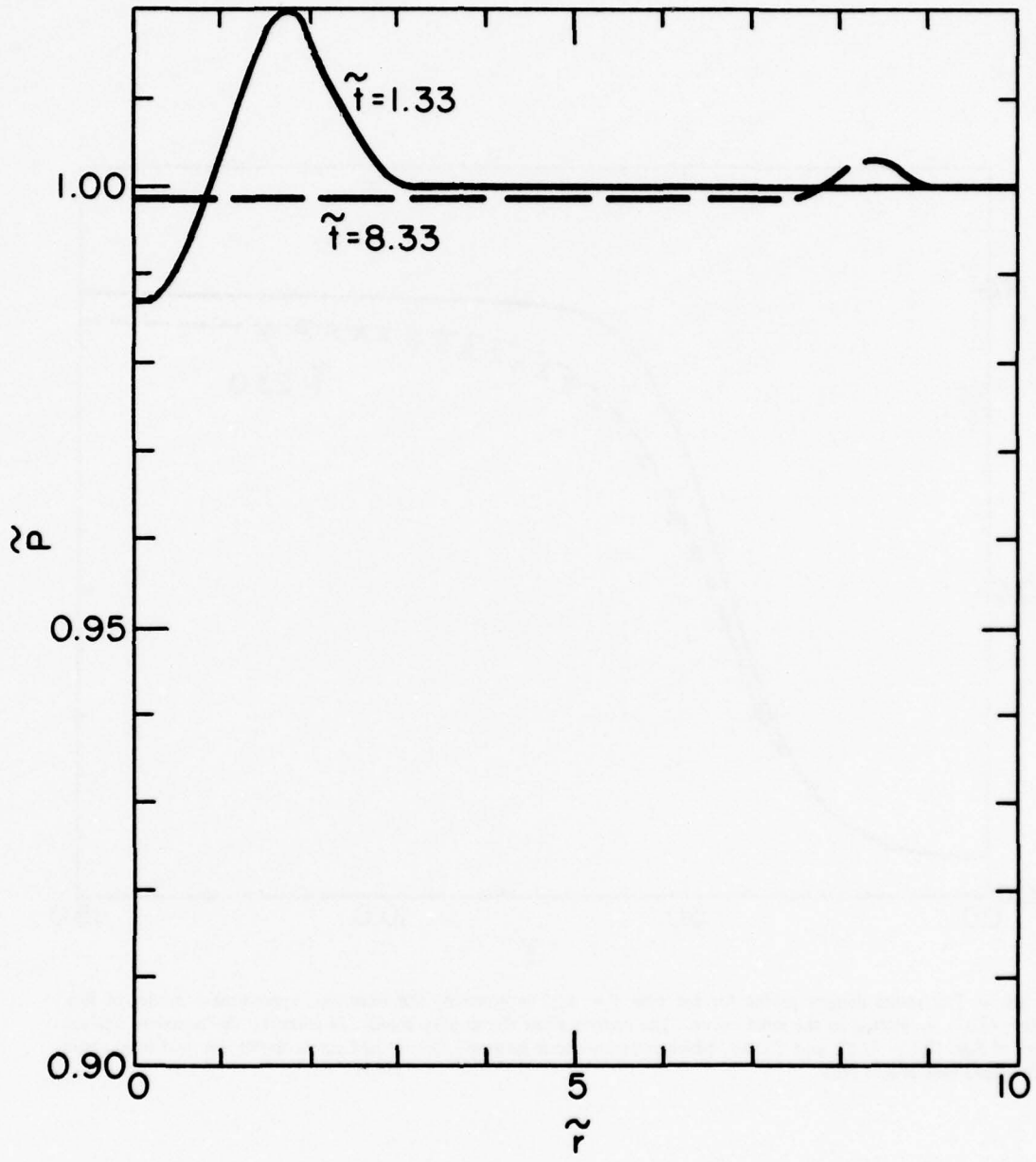


Fig. 2.8 — Radial distributions of the scaled pressure $\tilde{P}$, for a Bennett initial pressure distribution with initial overpressure $\tilde{P}_0 = 0.1$ at $\tilde{r} = 0$. Times are the same as Fig. 2.4.

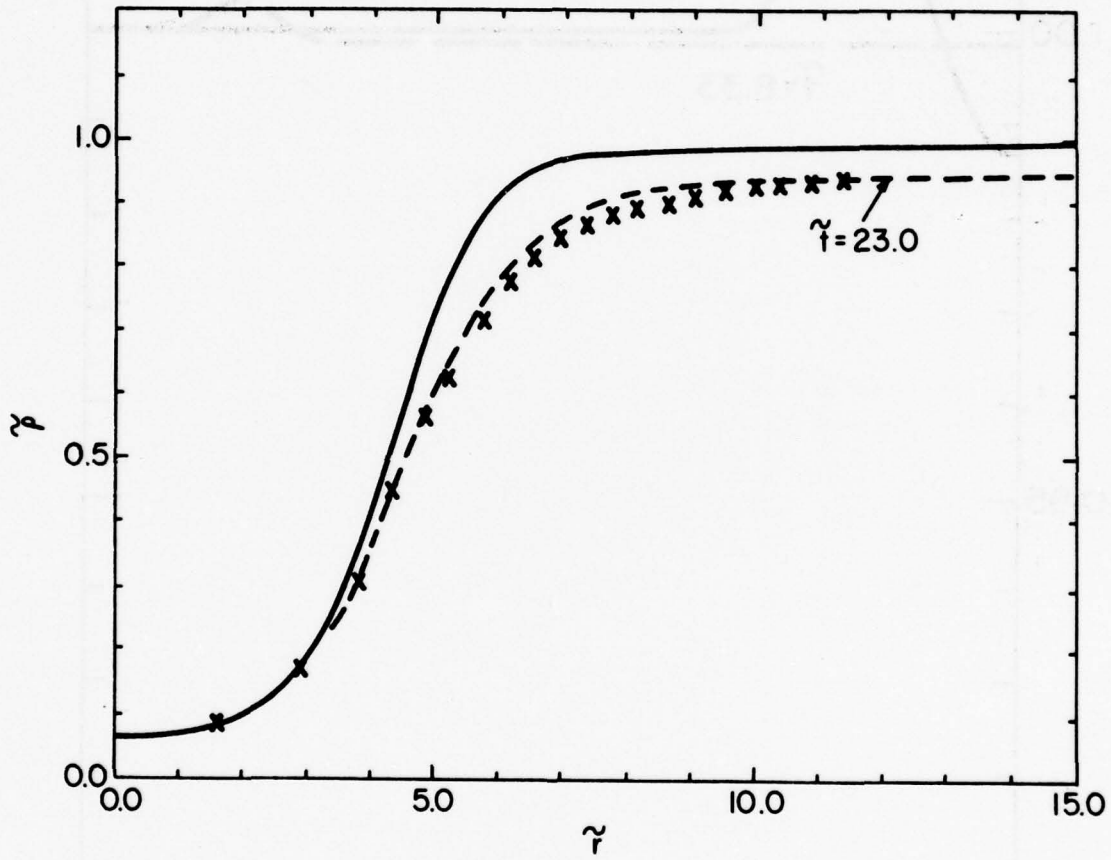


Fig. 2.9 — The radial density profile for the case $\tilde{P}$ = 42.0 as given by the isentropic approximate model of Eqs. (2.10c), (2.12), is plotted as the solid curve. The crosses show the density profile, as given by the complete analytic model of Eqs. (2.33), (2.8), and (2.10c), which includes shock heating. The dashed curve shows the fluid code result for the same case at late time.

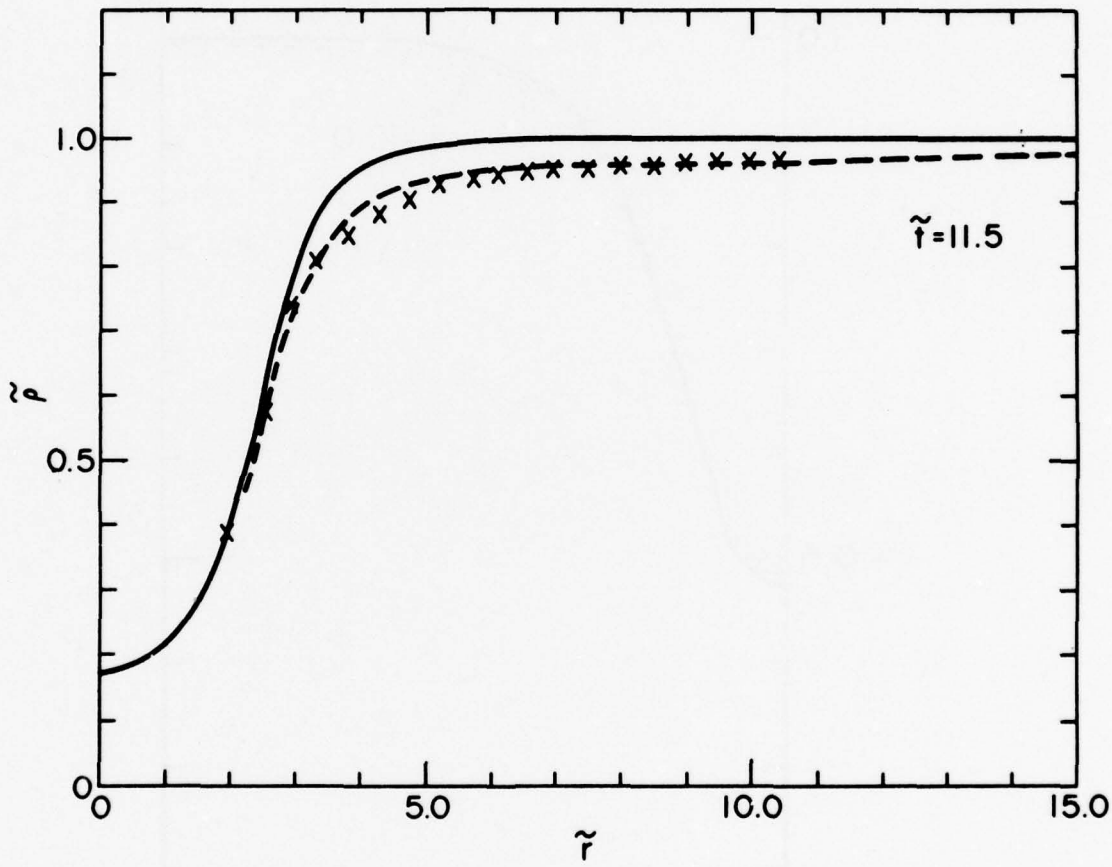


Fig. 2.10 — Similar to Fig. 2.9, but for $\tilde{P}_0 = 10.5$.

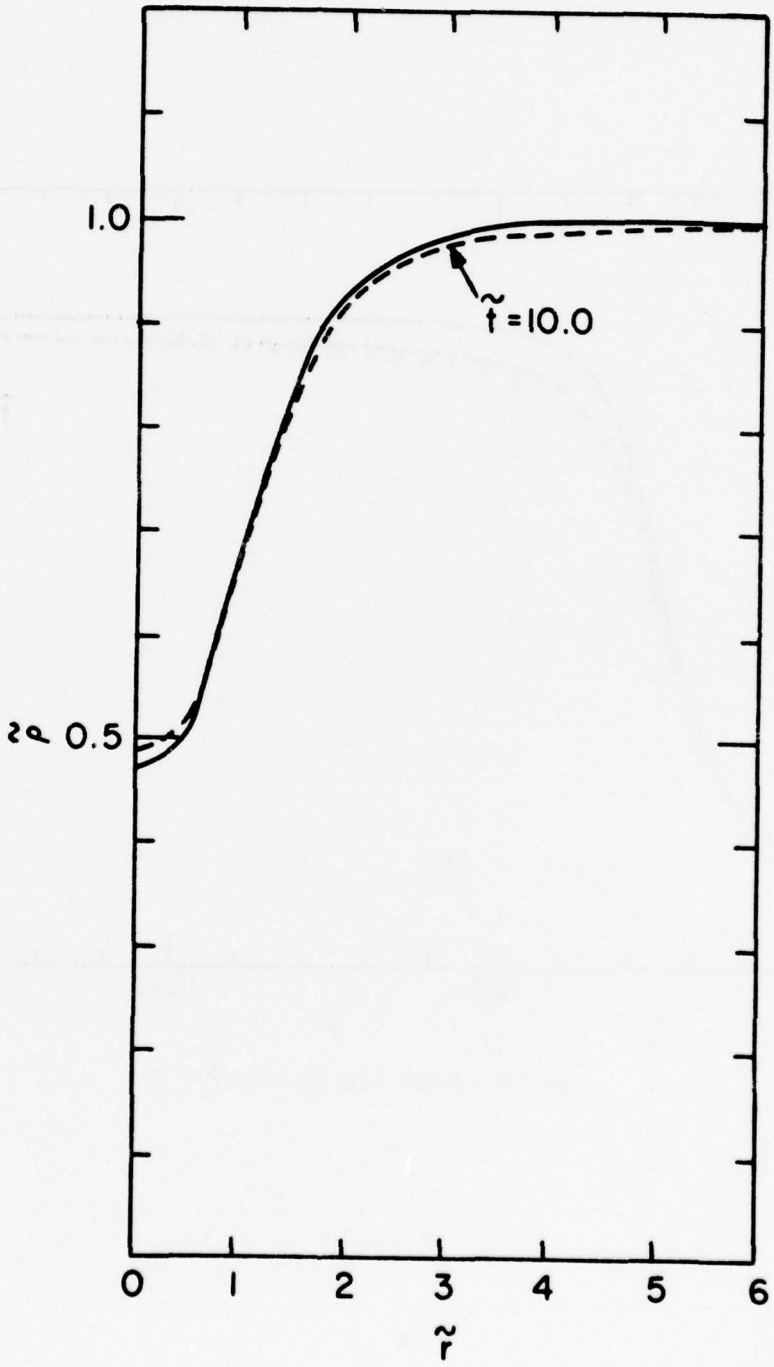


Fig. 2.11 — Similar to Fig. 2.9, but for $P_0 = 1.8$. Shock heating plays no significant role in this case of weak expansion.

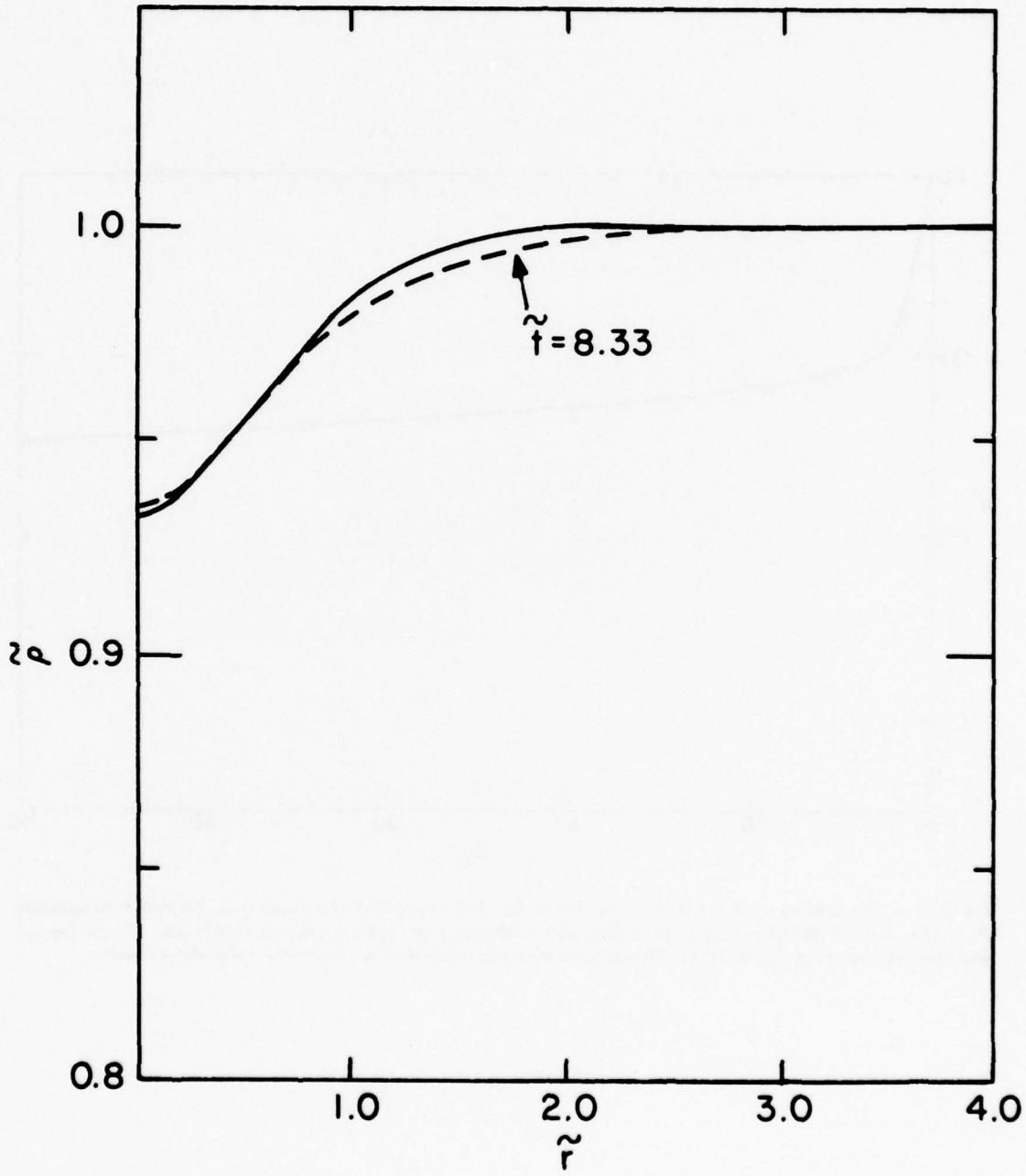


Fig. 2.12 — Similar to Fig. 2.11, but for $\tilde{P}_0 = 0.1$.

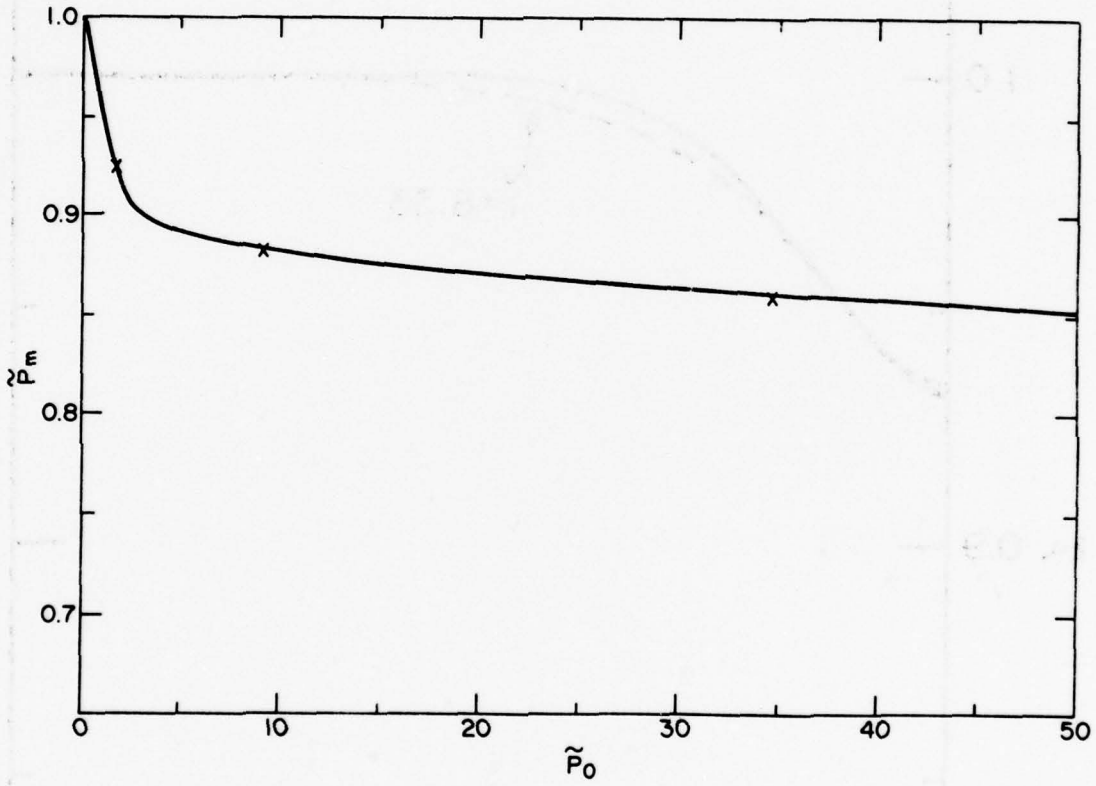


Fig. 2.13 — The solid curve is the pressure minimum $\hat{P}_m \equiv P_m/P_4$ plotted as a function of the initial overpressure $\tilde{P}_0 \equiv (P(r = 0, t = 0)/P_4) - 1$, as given by fluid code results for a first pulse in uniform ambient gas. The crosses are also fluid code values of $\tilde{P}_m$, for three different cases of energy deposition by a pulse in a preformed channel.

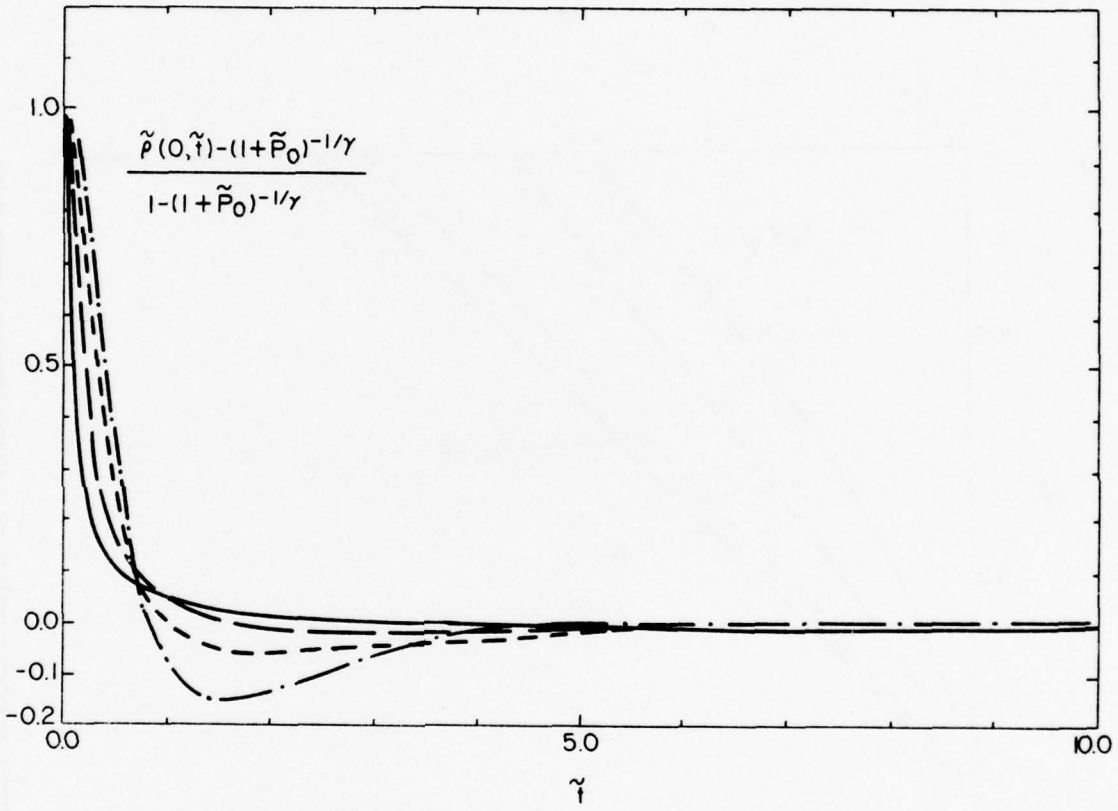


Fig. 2.14 — Time evolution of the quantity $[\tilde{\rho}(0,t) - (1 + \tilde{P}_0)^{-1}]/ [1 - (1 + \tilde{P}_0)^{-1}]$, as given by fluid code results, for four cases, $\tilde{P}_0 = 42.0$ (solid curve), 10.5 (long dashes), 1.8 (short dashes), and 0.1 (dot-dash). The vertical scale is the central density, plotted on a scale with initial value 1.0 and final value 0.0 for all cases.

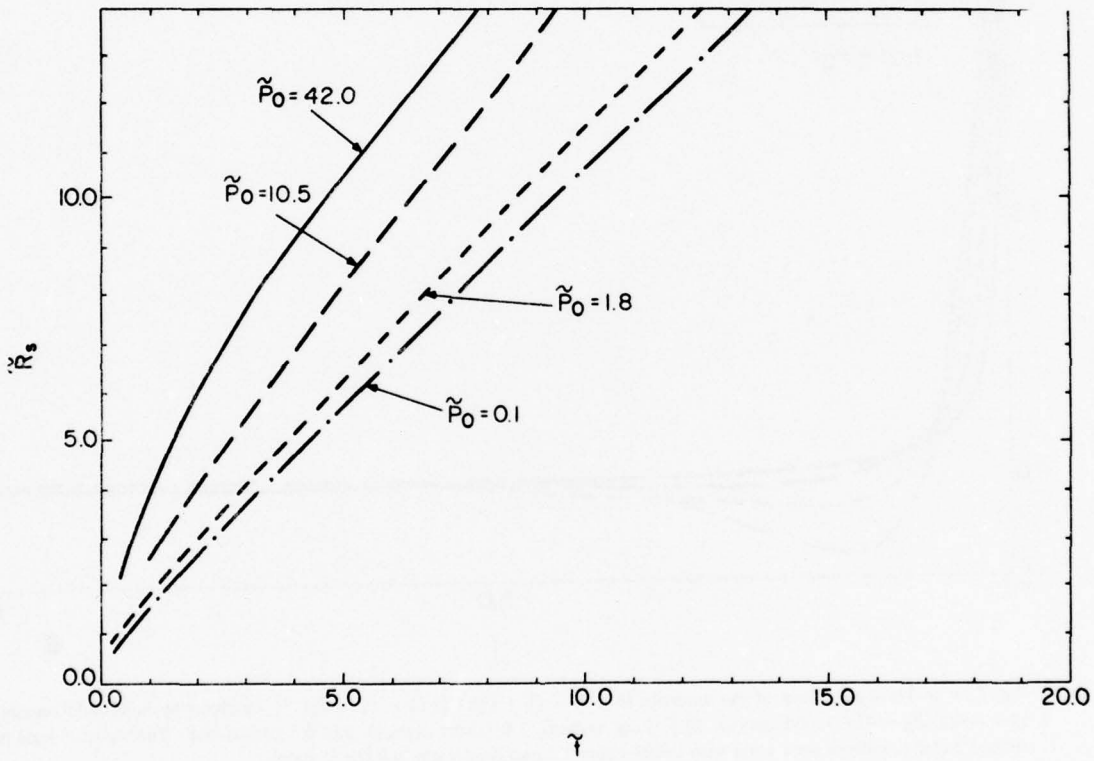


Fig. 2.15 — Location of the density peak (i.e., the shock location, if a shock has formed) for four cases, as given by the fluid code simulations.

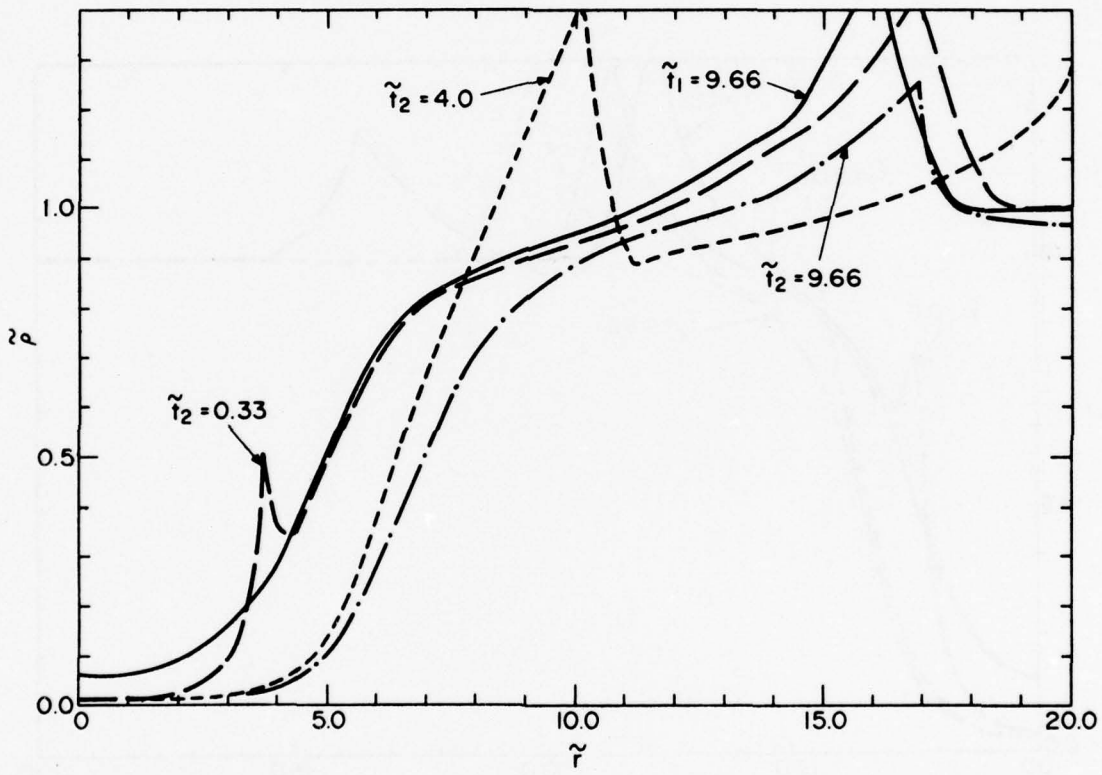


Fig. 3.1 — Radial profiles of the scaled density disturbance ($\tilde{\rho} \equiv \rho/\rho_4$). The solid curve shows the density profile at time $\tilde{t}_1 = 9.66$ following the passage of a first pulse with $\tilde{P}_{01} = 43.2$. The other curves show the disturbance at various times $\tilde{t}_2$ after the passage of a second pulse with overpressure $P_{02} = 34.9$. The times $\tilde{t}_2 = 0.33$, 40, and 9.66 are close to, respectively, the shock onset time, the time when the central pressure reaches the ambient value, and a time when the channel density is close to but slightly below its final equilibrium value.

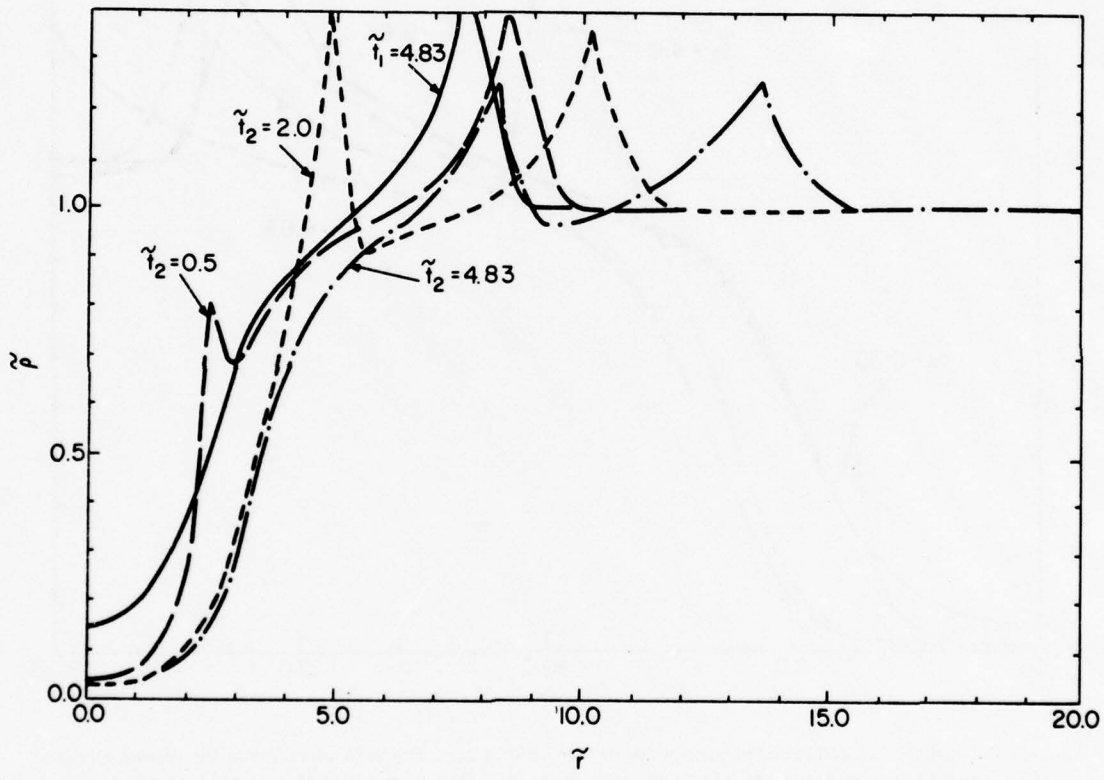


Fig. 3.2 — Similar to Fig. 3.1, but for a pulse with $\tilde{P}_{02} = 8.9$, propagating in a channel formed by a previous pulse with $\tilde{P}_{01} = 10.8$.

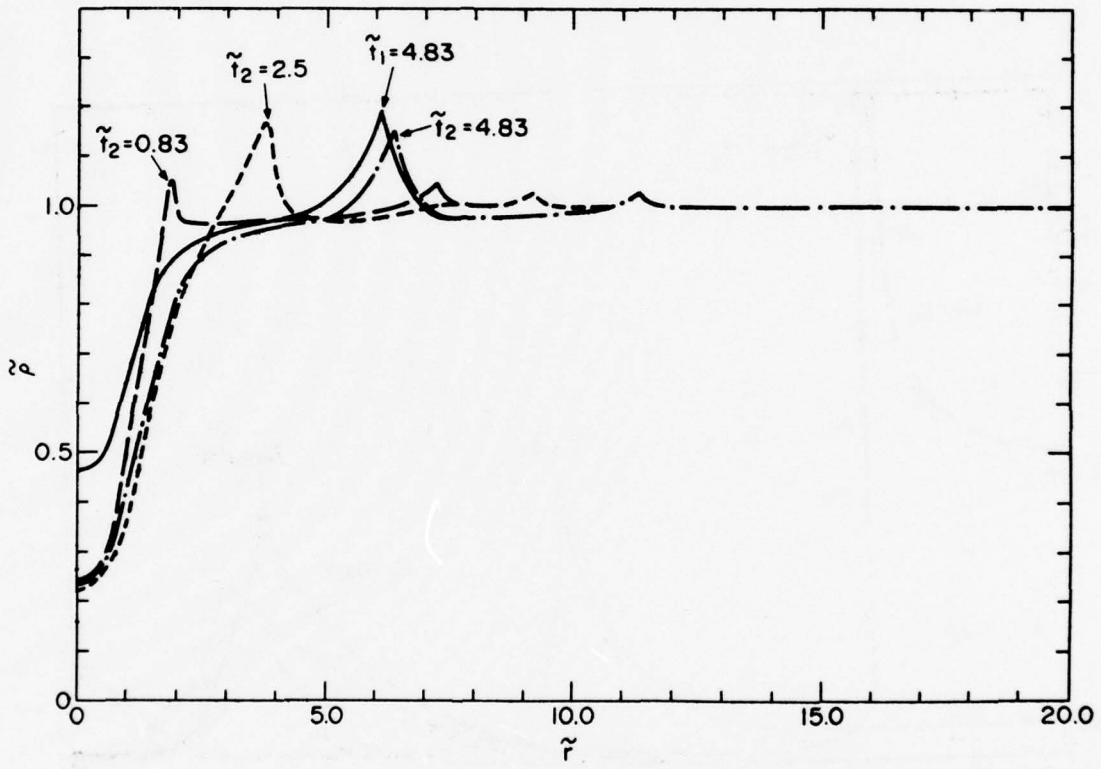


Fig. 3.3 — Similar to Fig. 3.1, but for a pulse with $\tilde{P}_{02} = 1.6$, propagating in a channel formed by a previous pulse with $\tilde{P}_{01} = 1.8$.

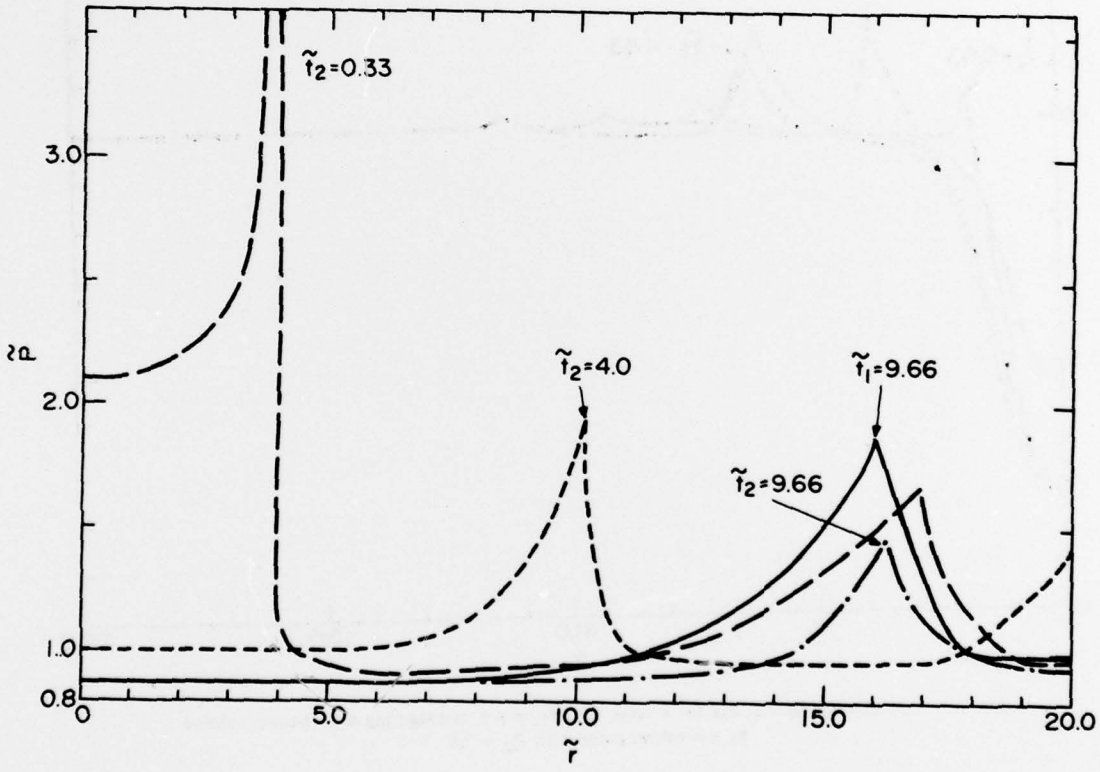


Fig. 3.4 — Radial profile of the scaled pressure ($\tilde{P} \equiv P/P_4$), at a time just before the passage of the second energy pulse (solid curve), and at various times after. Taken from the same fluid code simulation as Fig. 3.1.

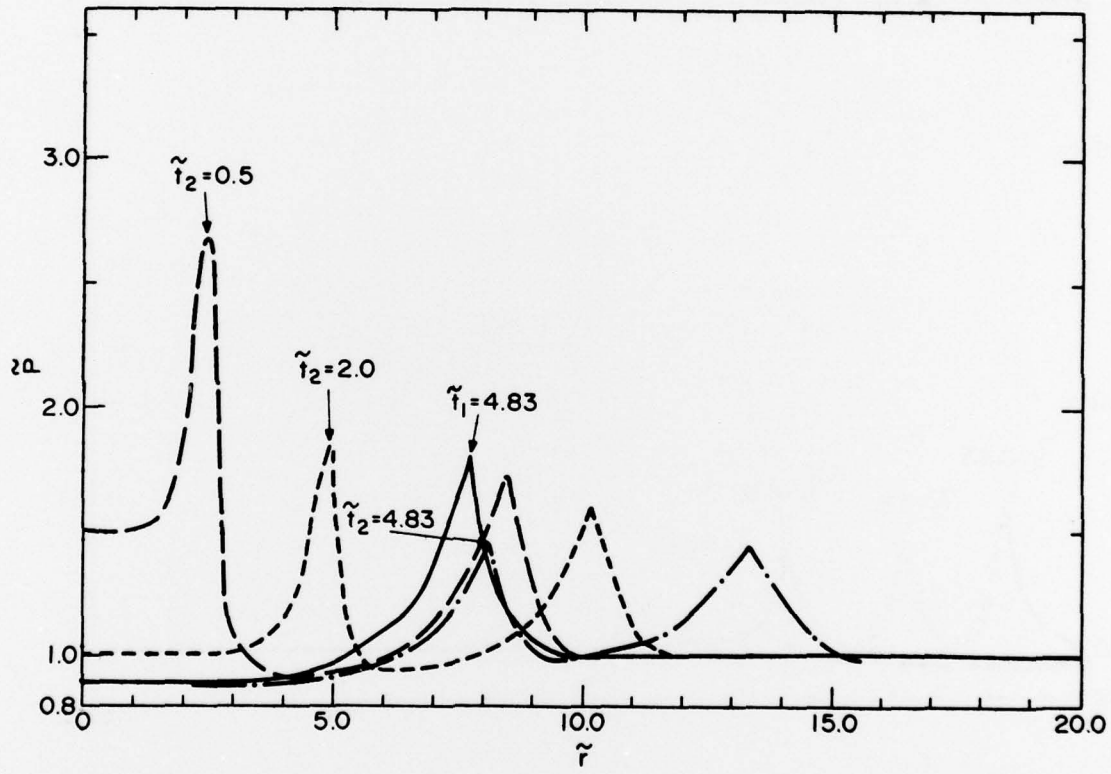


Fig. 3.5 — Radial profile of the scaled pressure $\tilde{P}$ at a time just before the passage of the second energy pulse (solid curve), and at various times after. Taken from the same fluid code simulations at Fig. 3.2.

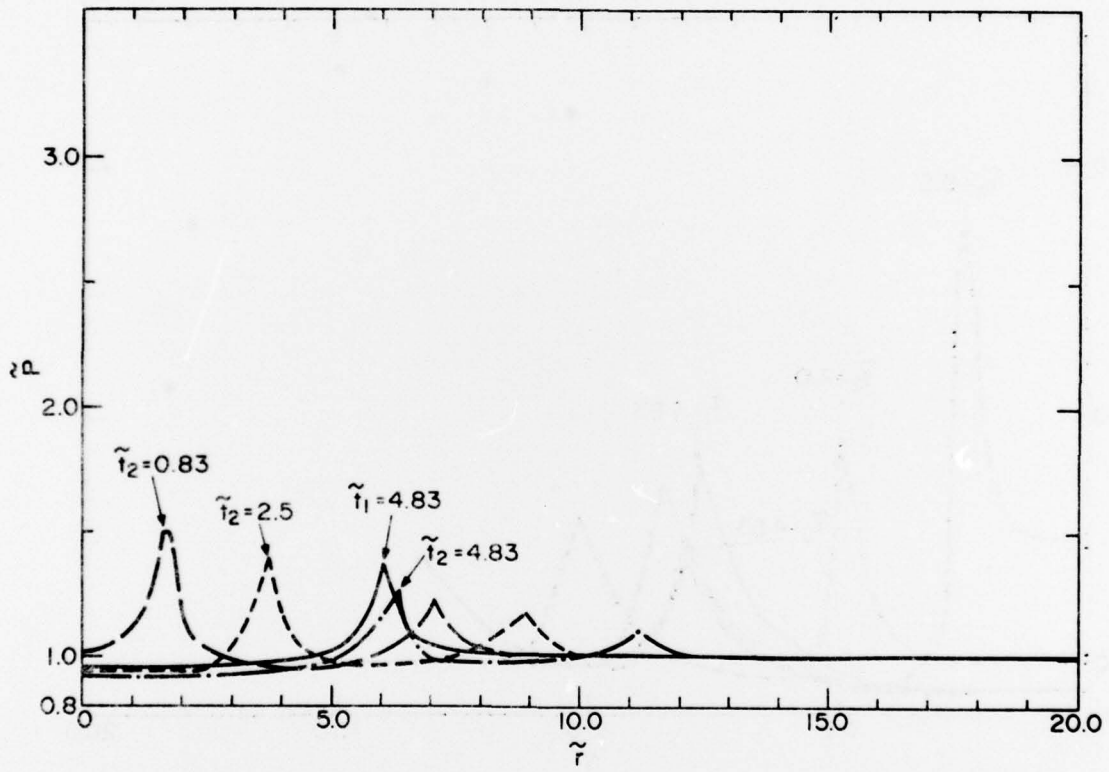


Fig. 3.6 — Radial profile of the scaled pressure $\tilde{\rho}$ at a time just before the passage of the second energy pulse (solid curve), and at various times after, taken from the same fluid code simulation as Fig. 3.3.

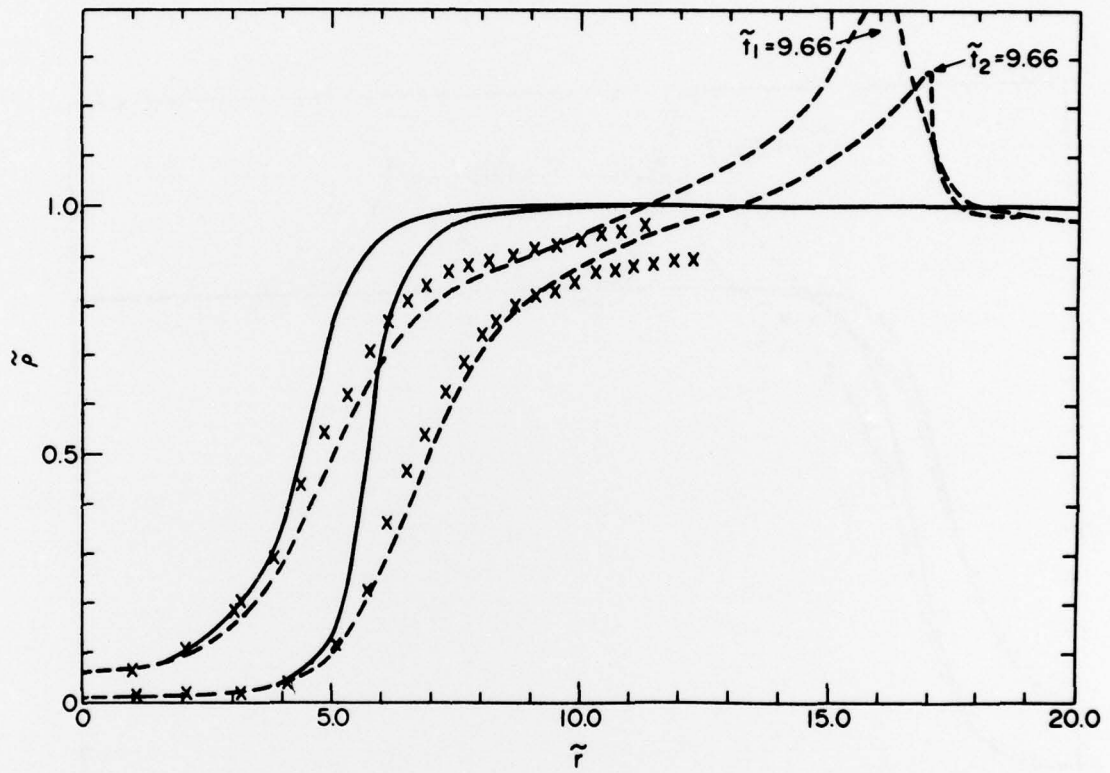


Fig. 3.7 — The radial profiles of the scaled density $\tilde{\rho}$ due to the first and the second pulses are shown for late time in dotted curves. The solid curves show the iteration results for two pulses obtained by the isentropic approximation. The crosses show the interation results for two pulses obtained from the complete analytic model, including the shock entropy production given by Eq. (3.9). The central overpressures produced initially by the two pulses are $\tilde{P}_{01}$ = 43.2 and $\tilde{P}_{02}$ = 34.9 (same fluid code simulation as Figs. 3.1 and 3.4).

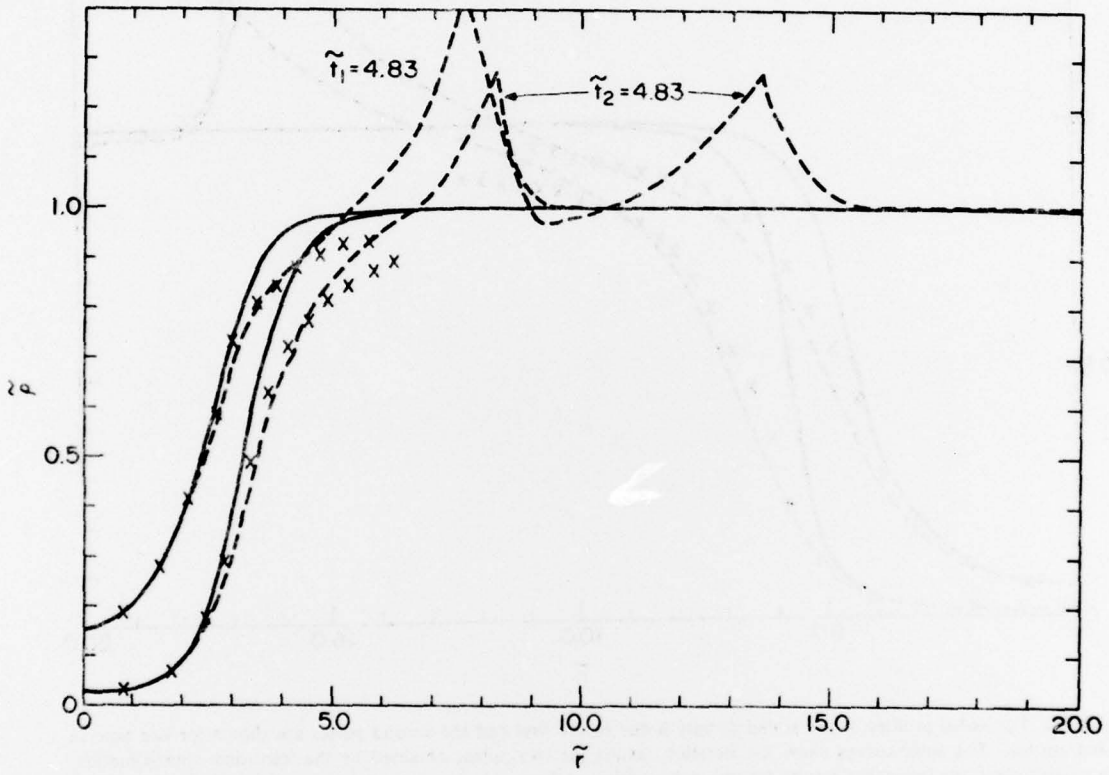


Fig. 3.8 — Similar to Fig. 3.7, but for two pulses producing initial overpressures $\tilde{P}_{01} = 10.8$ and $\tilde{P}_{02} = 8.9$. (Same fluid code simulation as Figs. 3.2 and 3.5)

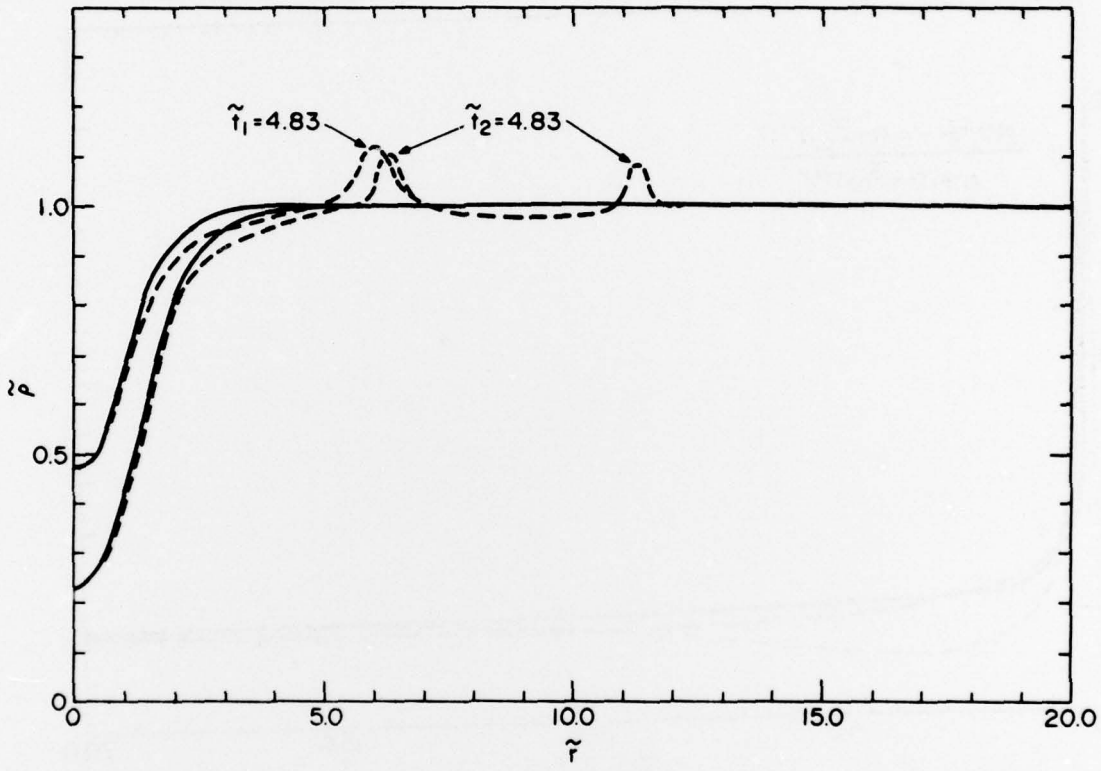


Fig. 3.9 — The dotted curves show the fluid code density profiles at late times, due to the first and second pulses producing overpressure $\tilde{P}_{01} = 1.81$ and $\tilde{P}_{02} = 1.6$. The solid curves show the iteration results obtained by the isentropic approximation. Shock heating plays no significant role in these weak expansions.

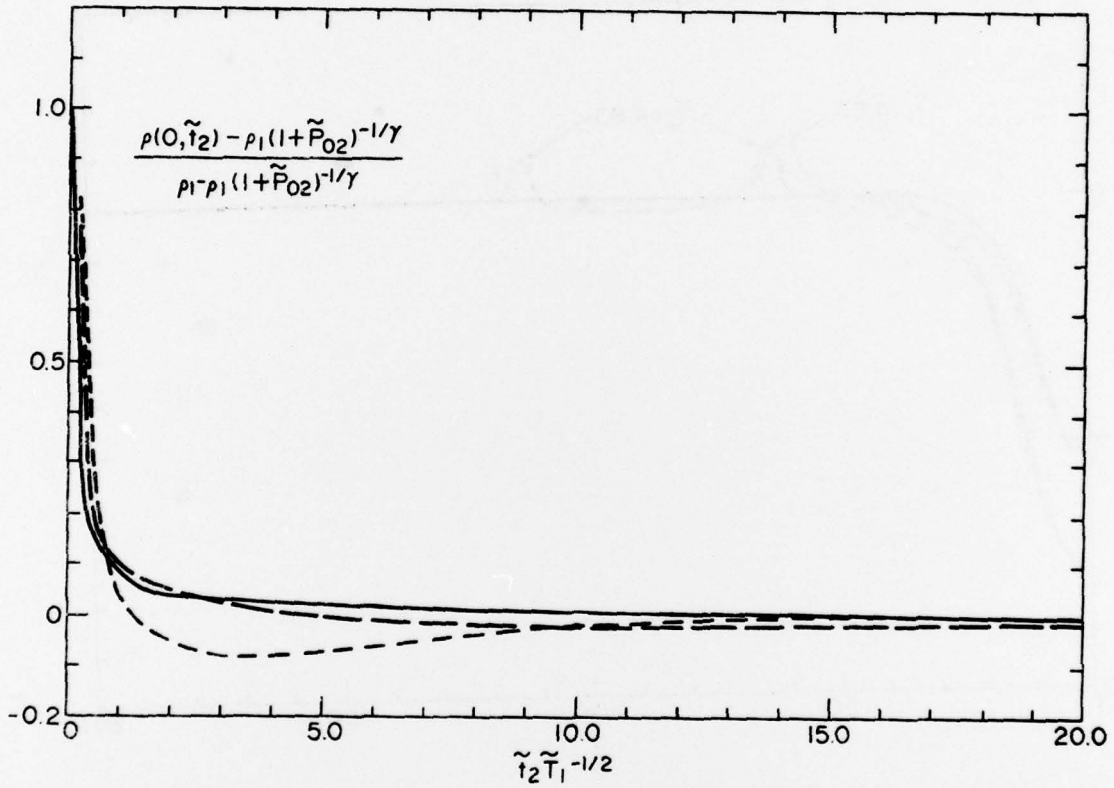


Fig. 3.10 — The time evolution of the central density, during expansion following the passage of a second pulse in a preformed channel. The three cases of Figs. 3.1, 3.2, and 3.3 are shown, i.e., respectively $\tilde{P}_{02} = 34.9$ (solid curve), 8.9 (long dashed) and 1.6 (short dashed). The vertical scale is chosen so that the initial value is 1.0 and the final value is zero in all cases. The time is scaled to a/c (0,0), where c(0,0) is the sound speed at $r = 0$ just before the second pulse arrives. The zero of time is when the second pulse arrives.

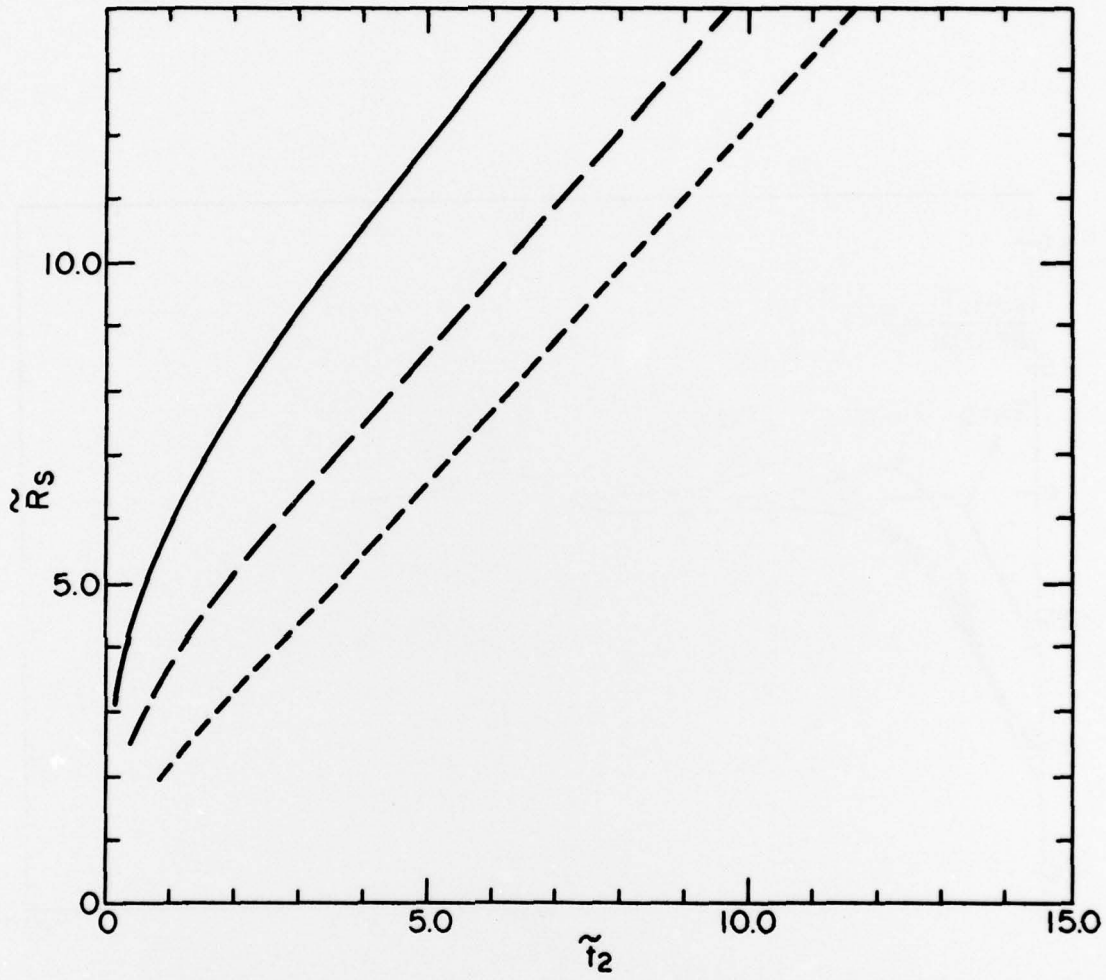


Fig. 3.11 — The location of the density peak (i.e., the shock location if a shock has formed), during expansion following the passage of a second pulse in a channel formed by a first pulse. The solid, long-dashed, and short-dahsed curves are for the fluid code simulations of Figs. 3.1, 3.2, and 3.3 respectively.

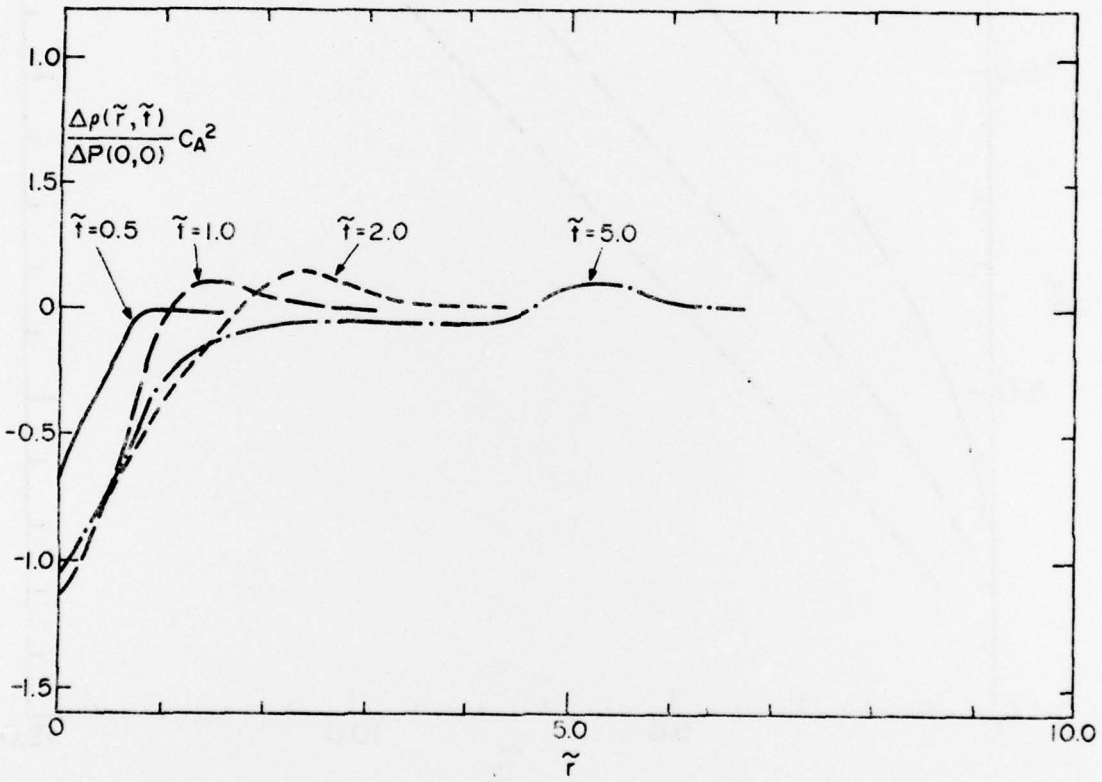


Fig. 4.1 — Radial profiles of the density perturbation at a sequence of times (Bennett initial overpressure profile).

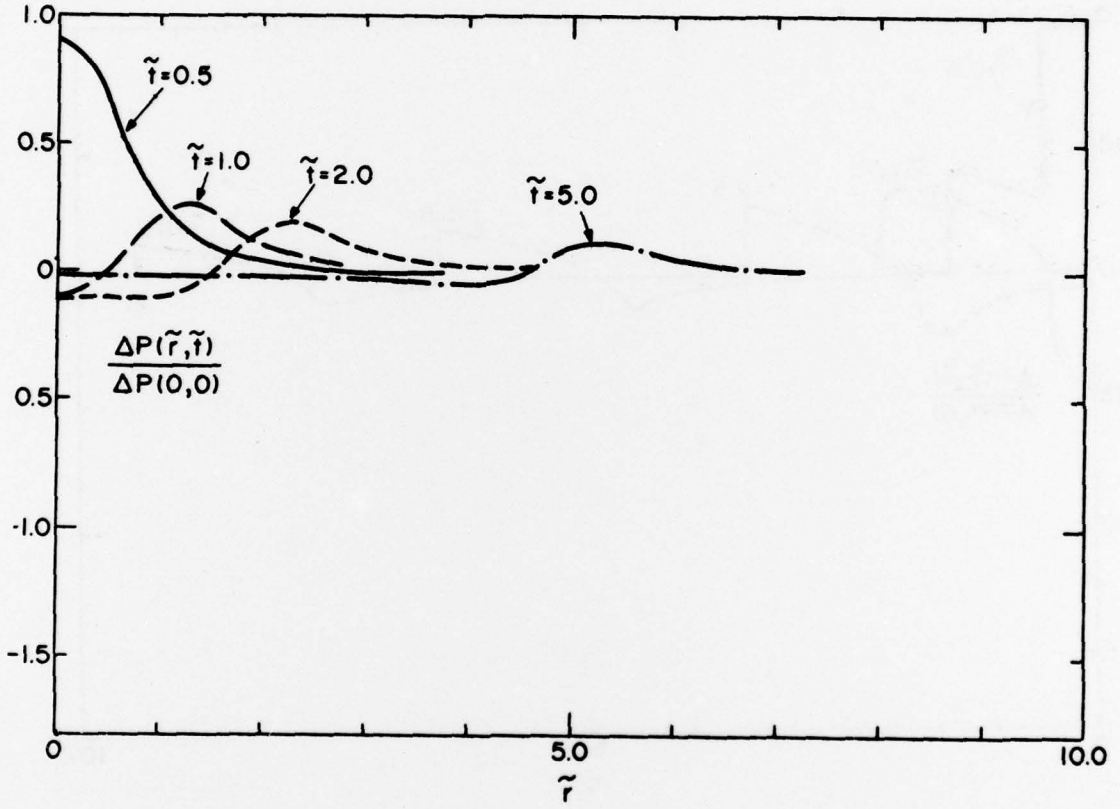


Fig. 4.2 — Radial profiles of the pressure perturbation at a sequence of times (Bennett initial overpressure profile).

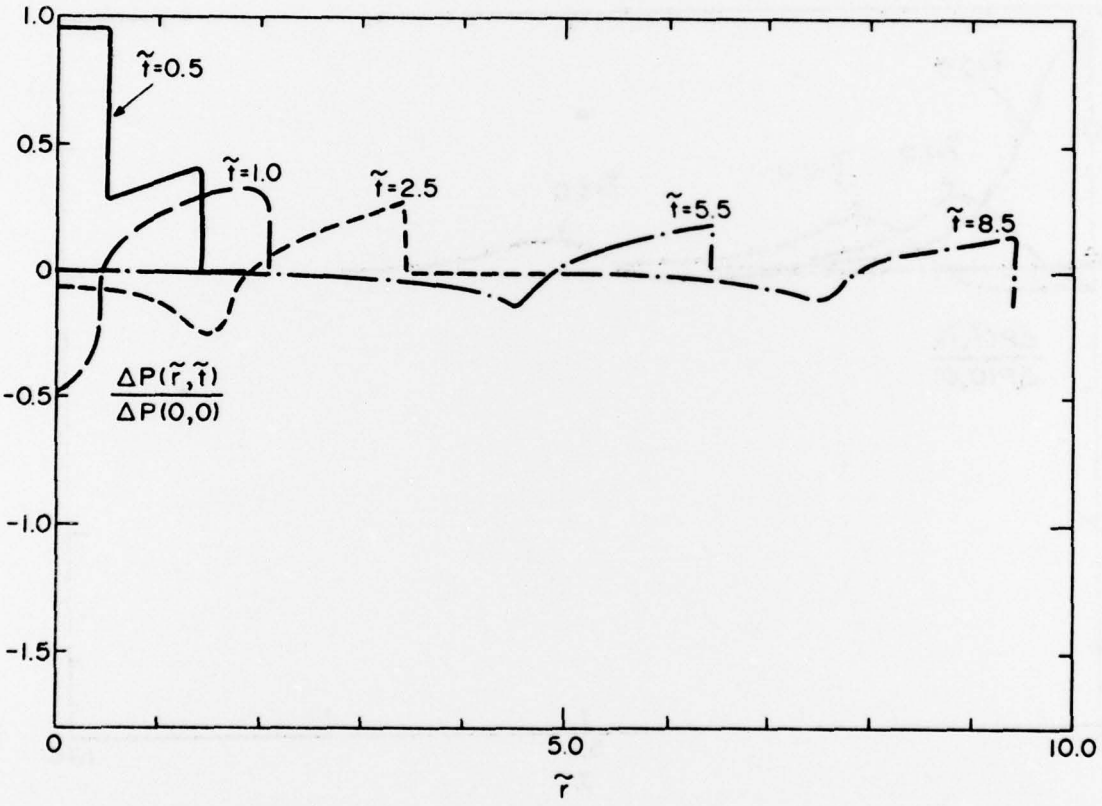


Fig. 4.3 — Radial profiles of the density perturbation at a sequence of times (step function initial overpressure profile).

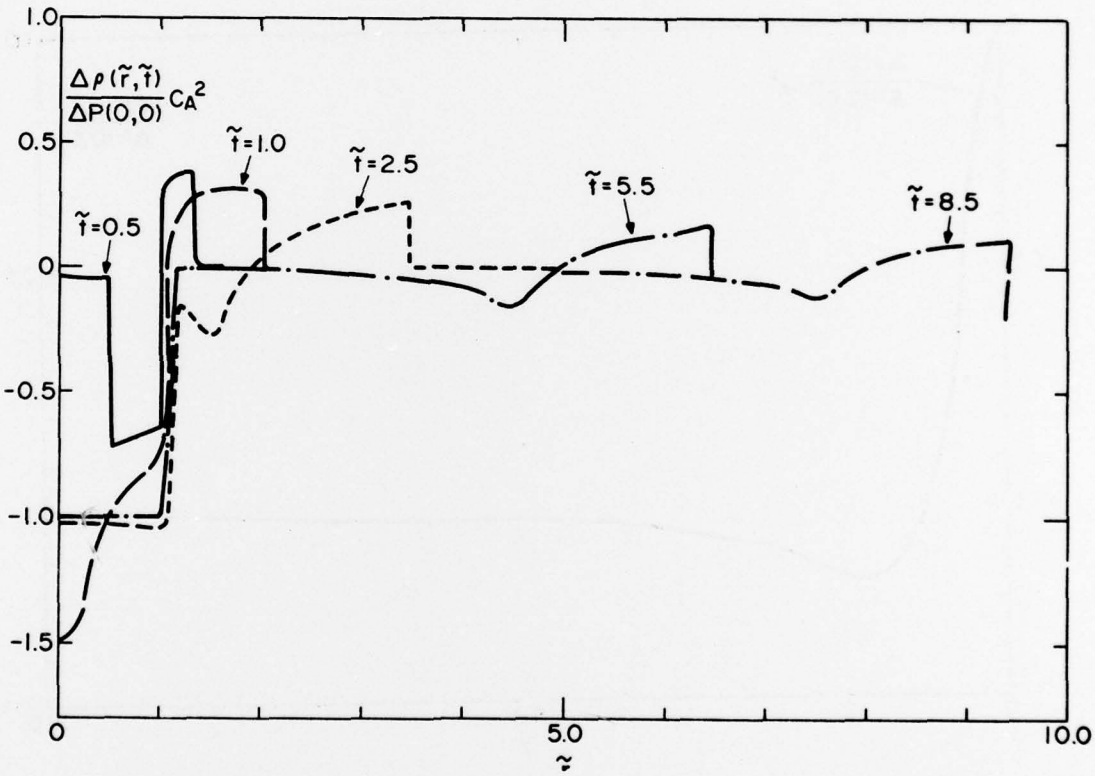


Fig. 4.4 — Radial profiles of the pressure perturbation at a sequence of times (step function initial overpressure profile).

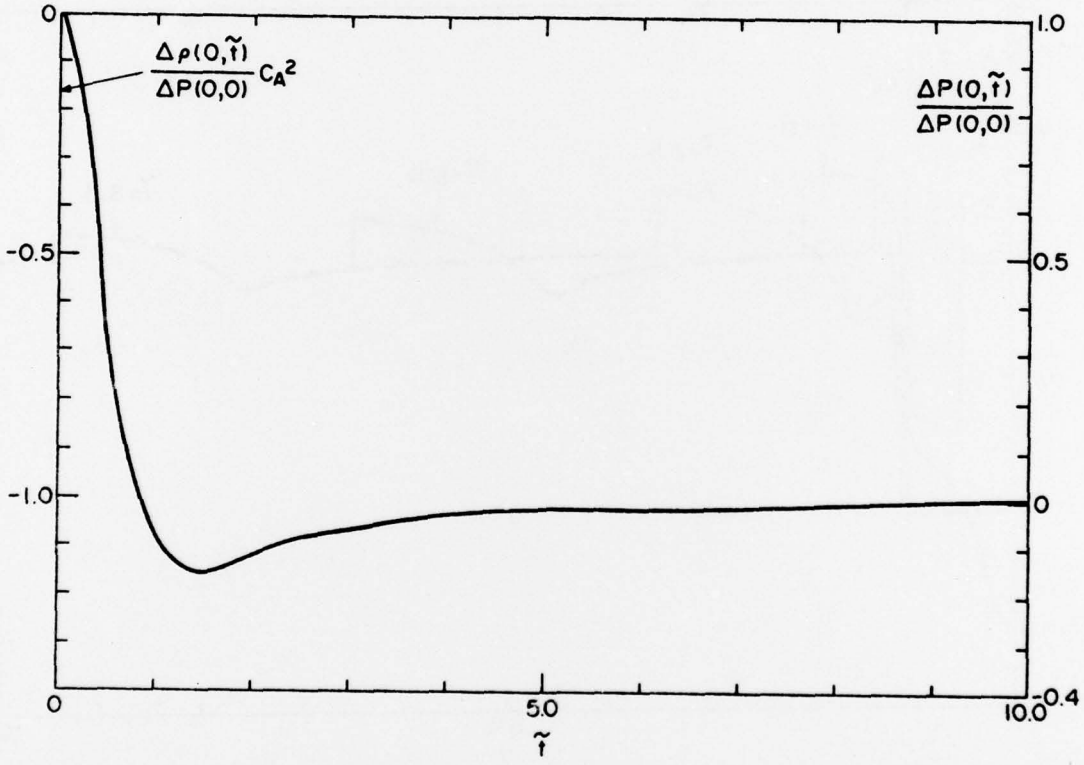


Fig. 4.5 — Time dependence of density perturbation and pressure perturbation at the origin, for Bennett initial overpressure profile (same curve, different vertical coordinates).

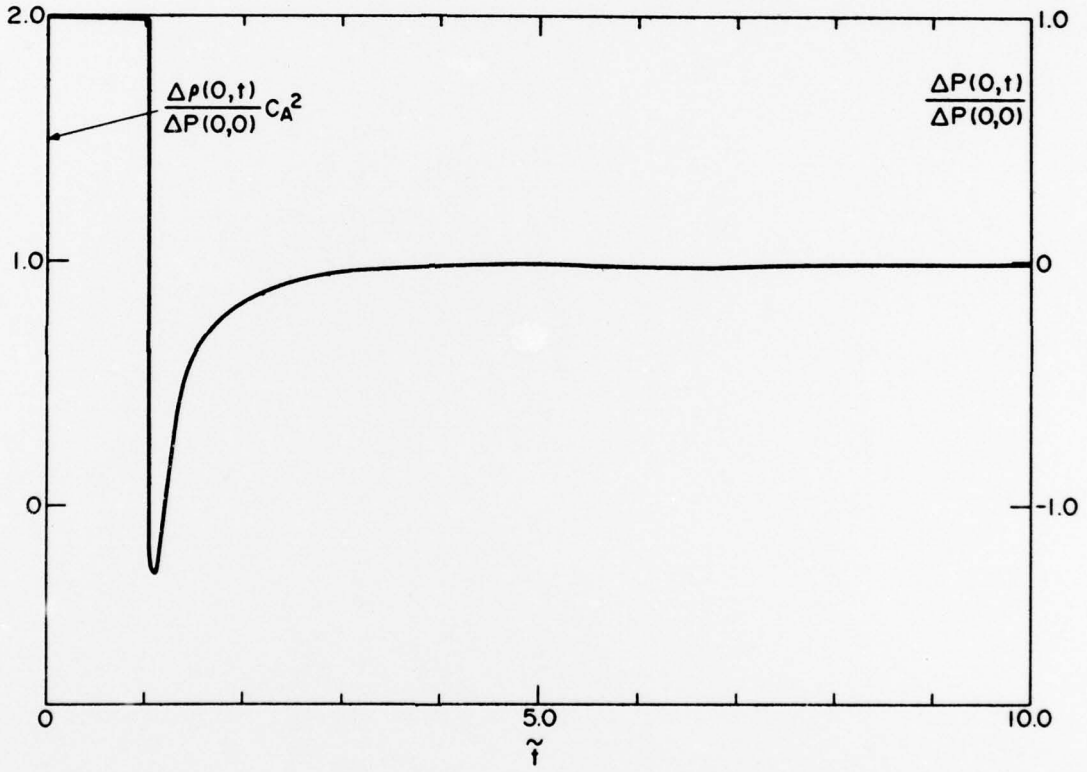


Fig. 4.6 — Time dependence of density perturbation and pressure perturbation at the origin, for step function initial overpressure profile (same curve, different vertical coordinate).